Low-power broadband solid-state MAS NMR of 14 N

Andrew J. Pell, Kevin J Sanders, Sebastian Wegner, Guido Pintacuda, Clare P. Grey

Low-power broadband solid-state MAS NMR of ^{14}N

Andrew J. Pell,[1,*] Kevin J. Sanders,[2] Sebastian Wegner,[3] Guido Pintacuda,[2] and Clare P. Grey[1]

[1]*Department of Chemistry, University of Cambridge, Lensfield Road, Cambridge, CB2 1EW, UK*[†]

[2]*Centre de RMN à Très Hauts Champs, Institut des Sciences Analytiques (CNRS, ENS Lyon, UCB Lyon 1), Université de Lyon, 69100 Villeurbanne, France*

[3]*Bruker BioSpin GmbH, D 76287 Rheinstetten, Germany*

Abstract

We propose two broadband pulse schemes for ^{14}N solid-state magic-angle-spinning nuclear magnetic resonance that achieve (i) complete population inversion, and (ii) efficient excitation of the double-quantum spectrum using low-power single-sideband-selective pulses. We give a comprehensive theoretical description of both schemes using a common framework that is based on the jolting-frame formalism of Caravatti et al. [J. Magn. Reson. 55, **88** (1983)]. This formalism is used to determine for the first time we can obtain complete population inversion of ^{14}N under low-power conditions, which we do here using single-sideband-selective adiabatic pulses. It is then used to predict that double-quantum coherences can be excited using low-power single-sideband-selective pulses. We then proceed to design a completely new experimental scheme for double-quantum excitation. The final double-quantum excitation pulse scheme is easily incorporated into other NMR experiments, as demonstrated here for double quantum–single quantum ^{14}N correlation spectroscopy, and ^{1}H–^{14}N dipolar HMQC experiments. These pulses and irradiation schemes are evaluated numerically using simulations on single crystals and full powders, as well experimentally on ammonium oxalate ($(NH_4)_2C_2O_4$) at moderate MAS, and glycine at ultra-fast MAS. The performance of these new NMR methods is found to be very high, with population inversion efficiencies of 100% and double-quantum excitation efficiencies of 30–50%, that are hitherto unprecedented for the low RF field amplitudes, up to the spinning frequency, that are used here.

*Electronic address: andrew.pell@mmk.su.se

†Present address: Department of Materials and Environmental Chemistry, Arrhenius Laboratory, Stockholm University, SE-106 91 Stockholm, Sweden

I. INTRODUCTION

Nitrogen is a highly-abundant and important element in many areas of chemistry, materials science, and biology. However despite the high natural abundance of 99.6% ^{14}N is not a nucleus that is commonly studied with solid-state nuclear magnetic resonance (NMR). Most of the difficulties are associated with the integer nuclear spin $I = 1$, which results in the frequencies of the two observable Zeeman transitions being split by a large first-order quadrupolar coupling interaction, giving spectra with large anisotropic broadening. The conventional one-dimensional spectra are therefore very broad, with the result that there is often significant overlap between the neighbouring resonances, and therefore low spectral resolution. Furthermore these spectra are, in any case, often difficult to excite and manipulate using the comparatively low radiofrequency (RF) field amplitudes that are typically available as a result of the low gyromagnetic ratio, a feature which also results in low sensitivity despite the high natural abundance. Taken together these observations represent significant barriers to the adoption of ^{14}N solid-state NMR as a routine method in analytical science. More succinctly we can summarize the relevant issues as (i) the ability to excite the broad spectra using low-power RF fields, and (ii) the resolution of multiple sites with broad overlapping signal components.

Advances in broadband solid-state NMR of ^{14}N include work on wideline NMR where WURST pulses are applied in combination with Carr–Purcell–Meiboom–Gill (CPMG) signal acquisition under static conditions [1, 2], which result in excitation windows of 100–1000 kHz. However under static conditions the signal is spread over a continuum of frequencies, resulting in low sensitivity. The use of magic-angle spinning (MAS) has the advantage of concentrating the signal into discretely-spaced sidebands, resulting in both higher sensitivity and reduced resonance overlap. Recently Vitzthum et al. have proposed the excitation of the broad ^{14}N spinning-sideband manifold using the delays alternating with nutation for tailored excitation (DANTE) pulse scheme [3]. However this is disadvantaged by the very small bandwidth for isotropic sites, which is often limited to only a few kHz [4].

On the other hand, in the field of paramagnetic solid-state MAS NMR substantial advances have been made in the development of broadband pulse schemes employing swept-frequency adiabatic pulses [5]. To date the most successful example is the short high-powered adiabatic pulse (SHAP) which employs a tanh/tan pulse [6] of short duration of the order of 10 μs and high RF field amplitudes of the order of 100 kHz [7]. This scheme has proved remarkably versatile, and

has been incorporated into more sophisticated pulse sequences such as CPMG to refocus inhomogeneous line broadening [8], transferred-echo double resonance (TEDOR) for ^{1}H–^{13}C correlation spectroscopy [9], and the adiabatic magic-angle turning (aMAT) experiment which removes the overlap between spinning-sideband manifolds originating from the shift anisotropy (SA) interactions [10]. However the necessity of using high power means that SHAPs are not optimal candidates for ^{14}N NMR. A second notable broadband pulse scheme is the single-sideband-selective adiabatic pulse (S^{3}AP), in which a low-power WURST [11] or hyperbolic secant [12] pulse irradiates a single sideband of the manifold. The resonance frequencies of the spin systems shift in and out of the pulse bandwidth during sample rotation, with the effect that the spin-state populations, and therefore the whole spinning-sideband manifold, are completely inverted [13]. This pulse scheme was first applied to the inversion of the satellite transition populations of half-integer quadrupolar nuclei [14–17], and has been more recently applied to spin $I = 1/2$ nuclei in paramagnetic systems, for which the first full theoretical description was given [18]. It has been shown that, in the best cases, complete inversion can be obtained when the width of the spinning-sideband manifold is an order of magnitude larger than the RF field amplitude.

Research into improving the resolution of ^{14}N solid-state MAS NMR has focussed on using additional nuclear-spin transitions. For example, indirect detection of the ^{14}N spectrum can be achieved from one-dimensional triple-resonance ^{1}H/^{13}C/^{14}N experiments incorporating transfer of populations in double resonance (TRAPDOR) [19, 20], two-dimensional heteronuclear multiple-quantum correlation (HMQC) experiments where the ^{14}N spin is coupled to a spin $I = 1/2$ such as ^{1}H or ^{13}C [21–27]. The signal separation comes from the increased spectral dispersion of the two-dimensional spectrum compared to the one-dimensional spectrum. Another method, which we focus on here, is the excitation of the double-quantum spectrum which is not broadened by the first-order quadrupolar interaction. The observation of the double-quantum spectrum can be done indirectly using TRAPDOR [19], a two-dimensional double-quantum–single-quantum correlation experiment such as those designed for ^{2}H MAS NMR [28], or a modified HMQC experiment [29]. A different, and intriguing, approach is to excite and observe the double-quantum spectrum directly via ^{14}N overtone spectroscopy [30, 31]. This method has the advantage of potentially allowing the double-quantum spectrum to be observed in a one-dimensional acquisition, but suffers from very low sensitivity.

In this paper we address the two issues of broadband inversion, and double-quantum excitation of ^{14}N. We begin by reviewing the jolting-frame model of Caravatti et al. which is the theoretical

framework used to model single-sideband-selective irradiation schemes [13]. We then extend this framework to S^3APs applied to ^{14}N solid-state NMR for broadband inversion, and show under which conditions they may be used for broadband coherence refocusing. It is also shown how this theoretical description has allowed us for the first time to systematically obtain complete low-power broadband population inversion of ^{14}N. We then exploit these findings to derive entirely new pulse schemes for low-power broadband ^{14}N double-quantum excitation. These schemes are then incorporated into two-dimensional NMR experiments for obtaining ^{14}N double quantum–single quantum homonuclear correlation spectra, and ^{1}H–^{14}N single quantum–double dipolar HMQC (D-DQ-HMQC) spectra. All of these methods are validated using a combination of numerical simulations on single crystals and powders, and experiments on powder samples of ammonium oxalate $(NH_4)_2C_2O_4$ at moderate MAS, and glycine at ultra-fast MAS, and are shown to achieve very high excitation and inversion efficiencies for the low RF powers employed, that have hitherto been unprecedented.

II. SPIN INTERACTIONS OF A NUCLEAR SPIN $I = 1$

In this section we review the first-order quadrupolar interaction under magic-angle spinning (MAS) for a nuclear spin $I = 1$. We pay particular attention to the form of the spinning sideband manifolds for crystallites of different orientations, as an appreciation of these is crucial to understanding the low-power pulse schemes.

A. Basis operators

The definition of the relevant Hamiltonians and density operator for a nuclear spin $I = 1$ is greatly facilitated by using a suitable set of basis operators. There are numerous bases that can be used, all of which should predict the same physics of a spin $I = 1$. However some bases can be used to highlight certain important features of the spin dynamics more readily than others. For this reason we here employ four different bases at different stages of the discussion in order to emphasise different points where needed. All four bases, their representations of the Hamiltonians and density operators, and transformation properties are given in detail in the SI, and are only outlined here.

In brief all four bases comprise nine basis operators. The first basis comprises the set of

single-element basis operators $|M_1\rangle\langle M_2|$ which are characterised by an order $p = M_1 - M_2$. The nine operators can be grouped into three projection operators $\hat{I}_{\mathrm{p}}^{(M)} = |M\rangle\langle M|$ with order $p = 0$ representing the populations of the three spin states, three coherence operators of positive order $\hat{I}_{+}^{(M_1,M_2)} = |M_1\rangle\langle M_2|$ with $M_1 > M_2$ comprising two single-quantum $p = +1$ operators and one double-quantum $p = +2$ operator, and three coherence operators of negative order $\hat{I}_{-}^{(M_1,M_2)} = |M_2\rangle\langle M_1|$ with $M_1 > M_2$ comprising two single-quantum $p = -1$ operators and one double-quantum $p = -2$ operator [32]. The second basis comprises nine Hermitian linear combinations of the Cartesian spin operators representing the nuclear spin along x, y, and z ($\hat{I}_x$, $\hat{I}_y$, and $\hat{I}_z$), and the identity operator $\hat{E}$ [33]. The third basis is the set of irreducible spherical-tensor operators $\hat{T}_{kp}$ with ranks 0, 1, and 2, and orders $-k \leq p \leq +k$. As for the single-element basis, the $\hat{T}_{kp}$ comprise three population operators with $p = 0$, two of order $p = +1$, two of order $p = -1$, and one each of orders $p = -2$ and $p = +2$ [34]. The final basis comprises a set of fictitious spin$-1/2$ operators that are defined as [35]:

$$\frac{1}{2}\hat{E}^{(M_1,M_2)} = \frac{1}{2}\left(\hat{I}_{\mathrm{p}}^{(M_1)} + \hat{I}_{\mathrm{p}}^{(M_2)}\right), \tag{1}$$

$$\hat{I}_{x}^{(M_1,M_2)} = \frac{1}{2}\left(\hat{I}_{+}^{(M_1,M_2)} + \hat{I}_{-}^{(M_1,M_2)}\right), \tag{2}$$

$$\hat{I}_{y}^{(M_1,M_2)} = \frac{1}{2\mathrm{i}}\left(\hat{I}_{+}^{(M_1,M_2)} - \hat{I}_{-}^{(M_1,M_2)}\right), \tag{3}$$

$$\hat{I}_{z}^{(M_1,M_2)} = \frac{1}{2}\left(\hat{I}_{\mathrm{p}}^{(M_1)} - \hat{I}_{\mathrm{p}}^{(M_2)}\right). \tag{4}$$

B. Nuclear quadrupole interaction

The quadrupolar coupling interaction is described by an anisotropic and symmetric tensor (spherical rank two) that is proportional to the electronic field gradient (EFG) tensor $\boldsymbol{V}$ [36, 37]. To first order as a perturbation to the Zeeman interaction, and under MAS, we write the Hamiltonian $\hat{H}_{\mathrm{q}}^{\mathrm{Q}}(\gamma_{\mathrm{QR}};t)$ as [38]

$$\hat{H}_{\mathrm{q}}^{\mathrm{Q}}(\gamma_{\mathrm{QR}};t) = W_{\mathrm{q}}^{\mathrm{Q}}(\gamma_{\mathrm{QR}};t)\left[\hat{I}_z^2 - \frac{1}{3}I(I+1)\hat{E}\right], \tag{5}$$

where $W_{\mathrm{q}}^{\mathrm{Q}}(\gamma_{\mathrm{QR}};t)$ is the orientational- and time-dependent quadrupolar splitting frequency. The orientational dependence is described by a set of Euler angles $\Omega_{\mathrm{QR}} = (\alpha_{\mathrm{QR}}, \beta_{\mathrm{QR}}, \gamma_{\mathrm{QR}})$ that specify the orientation of the principal axis frame (PAF) of the EFG tensor Q with respect to the rotor-fixed frame R, and the set of time-dependent Euler angles $\Omega_{\mathrm{RL}}(t) = (\omega_{\mathrm{r}}t, \beta_{\mathrm{RL}}, 0)$ which specify the

orientation of R in the laboratory frame L. We also define a carousel q that comprises all crystallites with the same α_{QR} and β_{QR}, but different γ_{QR} [39]. The quadrupolar splitting frequency is a sum of plane-wave functions:

$$W_{\mathrm{q}}^{\mathrm{Q}}(\gamma_{\mathrm{QR}};t) = \sum_{k=-2,k\neq 0}^{+2} w_{\mathrm{q}}^{(k)}(\gamma_{\mathrm{QR}}) \exp\left(-\mathrm{i}k\omega_{\mathrm{r}}t\right), \tag{6}$$

where ω_{r} is the spinning frequency, and the $w_{\mathrm{q}}^{(k)}(\gamma_{\mathrm{QR}})$ are a set of coefficients that depend on the Euler angles Ω_{QR} with the following expression:

$$w_{\mathrm{q}}^{(k)}(\gamma_{\mathrm{QR}}) = \sqrt{\frac{2}{3}}\frac{\omega_{\mathrm{Q}}}{eq}\sum_{l=-2}^{+l} \tilde{V}_{2l} \exp\left(-\mathrm{i}l\alpha_{\mathrm{QR}}\right) d_{lk}^{(2)}\left(\beta_{\mathrm{QR}}\right) d_{k0}^{(2)}\left(\beta_{\mathrm{RL}}\right) \exp\left(-\mathrm{i}k\gamma_{\mathrm{QR}}\right). \tag{7}$$

The quadrupolar splitting constant ω_{Q} is defined in terms of the quadrupolar coupling constant C_{Q} via the following expressions:

$$\omega_{\mathrm{Q}} = \frac{3\pi C_{\mathrm{Q}}}{2I(2I-1)}, \qquad C_{\mathrm{Q}} = \frac{e^2qQ}{h}, \tag{8}$$

where eq is the anisotropy of EFG tensor, and eQ is the nuclear quadrupole moment. The EFG anisotropy and asymmetry parameter η^{Q} are related to the Cartesian components of the EFG tensor in its PAF $\tilde{V}_{ii}$ according to:

$$eq = \tilde{V}_{zz}, \tag{9}$$

$$\eta^{\mathrm{Q}} = \frac{\tilde{V}_{xx} - \tilde{V}_{yy}}{\tilde{V}_{zz}}, \tag{10}$$

and the rank-two irreducible spherical tensor components in the PAF $\tilde{V}_{2l}$ are [40]:

$$\tilde{V}_{20} = \sqrt{\frac{3}{2}}eq, \tag{11}$$

$$\tilde{V}_{2\pm1} = 0, \tag{12}$$

$$\tilde{V}_{2\pm2} = \frac{1}{2}\eta^{\mathrm{Q}}eq. \tag{13}$$

The coefficients $w_{\mathrm{q}}^{(k)}(\gamma_{\mathrm{QR}})$ exhibit the following dependence on γ_{QR}:

$$w_{\mathrm{q}}^{(k)}(\gamma_{\mathrm{QR}}) = w_{\mathrm{q}}^{(k)}(0)\exp\left(-\mathrm{i}k\gamma_{\mathrm{QR}}\right). \tag{14}$$

C. The single-quantum spectrum and spinning-sideband manifold

During signal acquisition the density operator evolves between times t_1 and t_2 to acquire a phase $\Phi_{\mathrm{q}}^{\mathrm{Q}}(\gamma_{\mathrm{QR}}; t_2, t_1)$ that is given by

$$\Phi_{\mathrm{q}}^{\mathrm{Q}}(\gamma_{\mathrm{QR}}; t_2, t_1) = \int_{t_1}^{t_2} W_{\mathrm{q}}^{\mathrm{Q}}(\gamma_{\mathrm{QR}}; t)\mathrm{d}t \tag{15}$$

$$= \sum_{k=-2, k\neq 0}^{+2} \frac{w_{\mathrm{q}}^{(k)}(\gamma_{\mathrm{QR}})}{-\mathrm{i}k\omega_{\mathrm{r}}}\left[\exp\left(-\mathrm{i}k\omega_{\mathrm{r}}t_2\right) - \exp\left(-\mathrm{i}k\omega_{\mathrm{r}}t_1\right)\right]. \tag{16}$$

As shown in the SI, we can write the operator representing the total observable single-quantum coherence $\hat{I}_-$ in terms of the fictitious spin-1/2 operators $\hat{I}_-^{(+1,0)}$ and $\hat{I}_-^{(0,-1)}$, which represent the two observable coherences of order -1:

$$\hat{I}_- = \sqrt{2}\hat{I}_-^{(+1,0)} + \sqrt{2}\hat{I}_-^{(0,-1)}. \tag{17}$$

During evolution under the quadrupolar coupling Hamiltonian under MAS each of these two fictitious spin-1/2 operators acquires a phase of opposite sign, so that the overall transformation of $\hat{I}_-$ is

$$\hat{I}_- \rightarrow \sqrt{2}\exp\left(+\mathrm{i}\Phi_{\mathrm{q}}^{\mathrm{Q}}(\gamma_{\mathrm{QR}}; t, 0)\right)\hat{I}_-^{(+1,0)} + \sqrt{2}\exp\left(-\mathrm{i}\Phi_{\mathrm{q}}^{\mathrm{Q}}(\gamma_{\mathrm{QR}}; t, 0)\right)\hat{I}_-^{(0,-1)}. \tag{18}$$

The resulting single-crystallite time-domain signal $s_{\mathrm{q}}(\gamma_{\mathrm{QR}}; t)$ is

$$s_{\mathrm{q}}(\gamma_{\mathrm{QR}}; t) = \frac{\mathrm{Tr}\left[\hat{I}_+\left(\sqrt{2}\exp\left(+\mathrm{i}\Phi_{\mathrm{q}}^{\mathrm{Q}}(\gamma_{\mathrm{QR}}; t, 0)\right)\hat{I}_-^{(+1,0)} + \sqrt{2}\exp\left(-\mathrm{i}\Phi_{\mathrm{q}}^{\mathrm{Q}}(\gamma_{\mathrm{QR}}; t, 0)\right)\hat{I}_-^{(0,-1)}\right)\right]}{\mathrm{Tr}\left(\hat{I}_+\hat{I}_-\right)} \tag{19}$$

$$= \frac{1}{2}\exp\left(+\mathrm{i}\Phi_{\mathrm{q}}^{\mathrm{Q}}(\gamma_{\mathrm{QR}}; t, 0)\right) + \frac{1}{2}\exp\left(-\mathrm{i}\Phi_{\mathrm{q}}^{\mathrm{Q}}(\gamma_{\mathrm{QR}}; t, 0)\right) \tag{20}$$

$$= \cos\left(\Phi_{\mathrm{q}}^{\mathrm{Q}}(\gamma_{\mathrm{QR}}; t, 0)\right). \tag{21}$$

The two phase factors $\exp\left(\pm\mathrm{i}\Phi_\mathrm{q}^\mathrm{Q}(\gamma_\mathrm{QR};t,0)\right)$ are periodic over the rotor period, and so we can expand them as Fourier series [41]:

$$\exp\left(\pm\mathrm{i}\Phi_\mathrm{q}^\mathrm{Q}(\gamma_\mathrm{QR};t,0)\right) = \sum_{m=-\infty}^{+\infty} B_\mathrm{q}^{(m)} \exp\left(\pm\mathrm{i}\xi_\mathrm{q}^{(m)}(\gamma_\mathrm{QR})\right)\exp(\pm\mathrm{i}m\omega_\mathrm{r}t), \tag{22}$$

where the complex coefficients are given by

$$B_\mathrm{q}^{(m)} \exp\left(\pm\mathrm{i}\xi_\mathrm{q}^{(m)}(\gamma_\mathrm{QR})\right) = \frac{1}{\tau_\mathrm{r}}\int_0^{\tau_\mathrm{r}} \exp\left(\pm\mathrm{i}\Phi_\mathrm{q}^\mathrm{Q}(\gamma_\mathrm{QR};t,0)\right)\exp(\mp\mathrm{i}m\omega_\mathrm{r}t)\,\mathrm{d}t. \tag{23}$$

We see that each Fourier series is the complex conjugate of the other. The two series correspond to two spinning sideband manifolds, one for each of the two coherences of order -1, which are superimposed upon each other. The coherence $|0\rangle\langle+1|$ has a spinning-sideband manifold in which the mth-order sideband has intensity $B_\mathrm{q}^{(m)}$ and phase $\xi_\mathrm{q}^{(m)}(\gamma_\mathrm{QR})$. This sideband is coincident with the mth-order sideband of the other coherence $|-1\rangle\langle 0|$, which has intensity $B_\mathrm{q}^{(-m)}$ and phase $-\xi_\mathrm{q}^{(-m)}(\gamma_\mathrm{QR})$. Figure 1 (a) shows the energy levels of a spin $I = 1$, on which the two single-quantum coherences are marked. The resulting single-crystal spectra from each coherence are shown in Figure 1 (b). The spinning-sideband manifold of one coherence is related to the other by a reversal about the centreband. The overall signal resulting from the superposition of the two manifolds is

$$s_\mathrm{q}(\gamma_\mathrm{QR};t) = \sum_{m=-\infty}^{+\infty} \frac{B_\mathrm{q}^{(m)}}{2}\left[\exp\left(+\mathrm{i}\xi_\mathrm{q}^{(m)}(\gamma_\mathrm{QR})\right)\exp(+\mathrm{i}m\omega_\mathrm{r}t) + \exp\left(-\mathrm{i}\xi_\mathrm{q}^{(m)}(\gamma_\mathrm{QR})\right)\exp(-\mathrm{i}m\omega_\mathrm{r}t)\right] \tag{24}$$

$$= \sum_{m=-\infty}^{+\infty} B_\mathrm{q}^{(m)} \cos\left(\xi_\mathrm{q}^{(m)}(\gamma_\mathrm{QR}) + m\omega_\mathrm{r}t\right). \tag{25}$$

In the spectrum obtained by Fourier transformation of $s_\mathrm{q}(\gamma_\mathrm{QR};t)$, the total intensity at frequency $+m\omega_\mathrm{r}$ is the sum of the two sidebands at this frequency, namely $\left(B_\mathrm{q}^{(m)}/2\right)\exp\left(+\mathrm{i}\xi_\mathrm{q}^{(m)}(\gamma_\mathrm{QR})\right) + \left(B_\mathrm{q}^{(-m)}/2\right)\exp\left(-\mathrm{i}\xi_\mathrm{q}^{(-m)}(\gamma_\mathrm{QR})\right)$, from which we see that the spectrum is symmetric about the centreband $m = 0$.

We can elucidate an important symmetry property relating to the γ_QR-dependence of the sideband intensities and phases, as first described by Levitt [39]. The quadrupolar splitting frequency $W_\mathrm{q}^\mathrm{Q}(\gamma_\mathrm{QR};t)$ of a crystallite with Euler angle γ_QR at time t is related to the splitting frequency of a

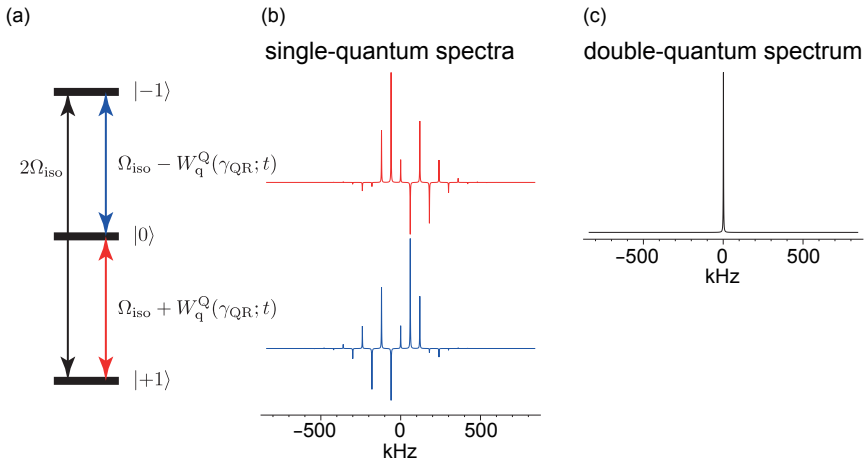

FIG. 1: The spin energy levels and single-crystal MAS NMR spectra of a nuclear spin $I = 1$ subject to a quadrupolar interaction and isotropic shift $\Omega_{\rm iso}$. The three spin energy levels are shown (a) with the two single-quantum coherences indicated in red and blue, and the double-quantum coherence shown in black. Representative examples of two simulated single-crystal MAS NMR spectra, one due to each single-quantum coherence, are shown in (b). We note that the spectrum due to one coherence can be reproduced from the other by reversing the frequency axis. The sum of these two spectra (not shown) is therefore symmetric about the centreband, here at zero frequency. The double-quantum coherence is unaffected by the quadrupolar interaction, and evolves at twice the isotropic shift. The corresponding double-quantum spectrum in (c) contains a single, sharp peak at $2\Omega_{\rm iso}$. The spin-interaction parameters are $\Omega_{\rm iso}$, $\omega_{\rm Q}/2\pi = 200$ kHz and $\eta_{\rm Q} = 0.3$. The crystallite orientation is specified by the Euler angles $\Omega_{\rm QR} = (0°, 45°, 0°)$ and the MAS frequency is 60 kHz.

different crystallite in the same carousel, but with $\gamma_{\rm QR} = 0$ as follows:

$$W_{\rm q}^{\rm Q}(\gamma_{\rm QR};t) = W_{\rm q}^{\rm Q}(0;t+\gamma_{\rm QR}/\omega_{\rm r}). \tag{26}$$

From this we can deduce the following symmetry relation pertaining to the phase $\Phi_{\rm q}^{\rm Q}(\gamma_{\rm QR};t,0)$:

$$\Phi_{\rm q}^{\rm Q}(\gamma_{\rm QR};t,0) = \Phi_{\rm q}^{\rm Q}(0;t+\gamma_{\rm QR}/\omega_{\rm r},0) - \Phi_{\rm q}^{\rm Q}(0;\gamma_{\rm QR}/\omega_{\rm r},0). \tag{27}$$

Substituting this into equation 22 we obtain

$$\begin{aligned}&\sum_{m=-\infty}^{+\infty} B_{\rm q}^{(m)}(\gamma_{\rm QR}) \exp\left(\pm {\rm i}\xi_{\rm q}^{(m)}(\gamma_{\rm QR})\right) \exp(\pm {\rm i}m\omega_{\rm r}t)\\ =&\sum_{m=-\infty}^{+\infty} B_{\rm q}^{(m)}(0) \exp\left(\pm {\rm i}\xi_{\rm q}^{(m)}(0)\right) \exp\left(\pm {\rm i}m(\gamma_{\rm QR}+\omega_{\rm r}t)\right) \exp\left(\mp {\rm i}\Phi_{\rm q}^{\rm Q}(0;\gamma_{\rm QR}/\omega_{\rm r},0)\right),\end{aligned} \tag{28}$$

from which we see that the sideband intensity is independent of γ_{QR}, and that the sideband phase has a well-defined γ_{QR} dependence:

$$B_{\mathrm{q}}^{(m)}(\gamma_{\mathrm{QR}}) = B_{\mathrm{q}}^{(m)}(0) \equiv B_{\mathrm{q}}^{(m)}, \tag{29}$$

$$\xi_{\mathrm{q}}^{(m)}(\gamma_{\mathrm{QR}}) = \xi_{\mathrm{q}}^{(m)}(0) - \Phi_{\mathrm{q}}^{\mathrm{Q}}(0; \gamma_{\mathrm{QR}}/\omega_{\mathrm{r}}, 0) + m\gamma_{\mathrm{QR}}. \tag{30}$$

Note that henceforth we denote the mth-order sideband intensity as $B_{\mathrm{q}}^{(m)}$, which reflects that it depends only on α_{QR} and β_{QR}, and not on γ_{QR}.

The spinning-sideband manifold in the spectrum of a powder can be calculated by averaging the time-domain function of a single crystallite $s_{\mathrm{q}}(\gamma_{\mathrm{QR}}; t)$ in equation 24 over all Euler angles Ω_{QR}. This is conveniently done in two steps: firstly we average $s_{\mathrm{q}}(\gamma_{\mathrm{QR}}; t)$ over γ_{QR} to obtain the time-domain signal $\overline{s}_{\mathrm{q}}(t)$ due to the complete carousel q:

$$\overline{s}_{\mathrm{q}}(t) = \frac{1}{2\pi} \int_0^{2\pi} s_{\mathrm{q}}(\gamma_{\mathrm{QR}}; t)\, \mathrm{d}\gamma_{\mathrm{QR}}; \tag{31}$$

secondly we average $\overline{s}_{\mathrm{q}}(t)$ over the remaining Euler angles α_{QR} and β_{QR} to give the time-domain signal from the whole powder $s(t)$:

$$s(t) = \frac{1}{4\pi} \int_0^{2\pi} \mathrm{d}\alpha_{\mathrm{QR}} \int_0^{\pi} \overline{s}_{\mathrm{q}}(t) \sin(\beta_{\mathrm{QR}})\, \mathrm{d}\beta_{\mathrm{QR}}. \tag{32}$$

The first average over γ_{QR} is computed by starting from equation 28, and expanding the phase factors $\exp\left(\mp \mathrm{i}\Phi_{\mathrm{q}}^{\mathrm{Q}}(0; \gamma_{\mathrm{QR}}/\omega_{\mathrm{r}}, 0)\right)$, as a Fourier series:

$$\exp\left(\mp \mathrm{i}\Phi_{\mathrm{q}}^{\mathrm{Q}}(0; \gamma_{\mathrm{QR}}/\omega_{\mathrm{r}}, 0)\right) = \sum_{n=-\infty}^{+\infty} B_{\mathrm{q}}^{(n)} \exp\left(\mp \mathrm{i}\xi_{\mathrm{q}}^{(n)}(0)\right) \exp(\mp \mathrm{i}n\gamma_{\mathrm{QR}}). \tag{33}$$

This gives the following expression for $s_{\mathrm{c}}(\gamma_{\mathrm{CR}}; t)$:

$$\begin{aligned} s_{\mathrm{q}}(\gamma_{\mathrm{QR}}; t) = & \frac{1}{2} \sum_{m,n} \Big[B_{\mathrm{q}}^{(m)} B_{\mathrm{q}}^{(n)} \exp\left(\mathrm{i}\left(\xi_{\mathrm{q}}^{(m)}(0) - \xi_{\mathrm{q}}^{(n)}(0)\right)\right) \exp\left(\mathrm{i}(m-n)\gamma_{\mathrm{QR}}\right) \exp\left(\mathrm{i}m\omega_{\mathrm{r}}t\right) \\ & + B_{\mathrm{q}}^{(m)} B_{\mathrm{q}}^{(n)} \exp\left(-\mathrm{i}\left(\xi_{\mathrm{q}}^{(m)}(0) - \xi_{\mathrm{q}}^{(n)}(0)\right)\right) \exp\left(-\mathrm{i}(m-n)\gamma_{\mathrm{QR}}\right) \exp\left(-\mathrm{i}m\omega_{\mathrm{r}}t\right) \Big]. \end{aligned} \tag{34}$$

Following the average over γ_{QR} according to equation 31 the only non-zero terms are those with

$m = n$, and we obtain the following time-domain signal for the carousel:

$$\overline{s}_{\mathrm{q}}(t) = \frac{1}{2}\sum_{m}\left[\left(B_{\mathrm{q}}^{(m)}\right)^2 + \left(B_{\mathrm{q}}^{(-m)}\right)^2\right]\exp\left(\mathrm{i}m\omega_{\mathrm{r}}t\right). \tag{35}$$

We see that all sidebands have the same phase, here zero, and that the intensity of the mth-order sideband is equal to the average of the squares of the two single-crystal sideband intensities from to the two coherences: $\left(B_{\mathrm{q}}^{(m)}\right)^2/2 + \left(B_{\mathrm{q}}^{(-m)}\right)^2/2$ [39]. The second average over α_{QR} and β_{QR} is conceptually straightforward. The result is a spinning sideband manifold

$$s(t) = \sum_{m} I^{(m)}\exp\left(\mathrm{i}m\omega_{\mathrm{r}}t\right), \tag{36}$$

where $I^{(m)}$ is given by the double integral

$$I^{(m)} = \frac{1}{4\pi}\int_0^{2\pi}\mathrm{d}\alpha_{\mathrm{QR}}\int_0^{\pi}\frac{1}{2}\left[\left(B_{\mathrm{q}}^{(m)}\right)^2 + \left(B_{\mathrm{q}}^{(-m)}\right)^2\right]\sin\left(\beta_{\mathrm{QR}}\right)\,\mathrm{d}\beta_{\mathrm{QR}}. \tag{37}$$

D. The double-quantum spectrum

The double-quantum spectrum has a very different appearance to the conventional single-quantum spectrum. The coherence, which is illustrated on the spin-level diagram in Figure 1 (a), is represented by the operator $\hat{I}_{-}^{(+1,-1)}$. As shown in the SI, this operator commutes with the quadrupolar interaction Hamiltonian in equation 5, and so does not evolve under this interaction:

$$\hat{I}_{-}^{(+1,-1)} \rightarrow \hat{I}_{-}^{(+1,-1)}. \tag{38}$$

The FID therefore contains a single frequency component that evolves at the isotropic shift, here equal to zero, and the corresponding spectrum contains a single sharp line with no spinning sidebands. An example spectrum is shown in Figure 1 (c).

III. LOW-POWER IRRADIATION OF SPINS SUBJECT TO LARGE ANISOTROPIC INTERACTIONS

We now turn to the principal topic of this paper, which is the description of low-power pulses acting on isolated spins $I = 1$ that are subject to large quadrupolar interactions. The definition of

low power is such that the peak radiofrequency (RF) field amplitude of the pulse satisfies $|\omega_1| < |\omega_r|$, and in the present case the term 'large quadrupolar interaction' means $\left|\omega_Q\right| \gg |\omega_r|$.

A. The jolting frame

It was shown by Caravatti et al. that low-power RF pulses applied to spins subject to large chemical-shift anisotropies (CSA) can be described very conveniently in a so-called jolting reference frame [13], which is the interaction frame of the anisotropic spin interaction(s). Here we use the term CSA to refer to the conventional orbital contribution to the total shift, which is found both in diamagnetic and paramagnetic systems. The more general term shift anisotropy (SA) is used for other contributions to the anisotropic part of the shift tensor, such as those due to unpaired electrons in paramagnetic systems. We have recently shown that this formalism can be used to model low-power pulse schemes applied to spins-1/2 with large CSA or paramagnetic SA interactions in order to describe single-sideband-selective adiabatic inversion pulses (S^3APs) [18], single-crystallite-selective (XS) pulse trains [42], and step-wise acquisition of spectra that are broader than the probe bandwidth via frequency stepping [43]. The aim of this section is to extend the jolting-frame treatment to spin $I = 1$ quadrupolar nuclei subject to the quadrupolar coupling interaction.

The basic idea is that the pulse has an RF field amplitude and bandwidth that is significantly smaller than the size of the anisotropic interaction. In addition the resonance frequencies due to the latter change constantly as a result of the MAS modulation, and so are shifting in and out of the pulse bandwidth during the pulse. The result is that the pulse is resonant with the spin system for only a fraction of the pulse duration. This fraction of time, and therefore the effect of the pulse on the spin, are quantifiable in the jolting frame.

We start with the standard rotating-frame Hamiltonian $\hat{H}(t)$ describing an isolated spin $I = 1$ subject to an anisotropic interaction under MAS, and which is experiencing RF irradiation:

$$\hat{H}(t) = \hat{H}_0(t) + \hat{H}_1(t). \tag{39}$$

The system Hamiltonian $\hat{H}_0(t)$ describes the anisotropic interaction, here the quadrupolar interaction Hamiltonian in equation 5. The RF pulse is described by a time-dependent amplitude $\omega_1(t)$

and phase $\phi_1(t)$, and is represented by the term $\hat{H}_1(t)$ which has the form

$$\hat{H}_1(t) = \omega_1(t)\hat{R}_z\left(\phi_1(t)\right)\hat{I}_x\hat{R}_z\left(\phi_1(t)\right)^{-1}, \tag{40}$$

where $\hat{R}_a(\theta)$ is the rotation operator representing a rotation of the spin about an axis defined by $\hat{I}_a$ through angle θ. The pulse phase is equal to the sum of two parts, namely a term $\omega_{\mathrm{tx}}t$ which sets the 'base' transmitter frequency at ω_{tx} relative to the receiver reference frequency, and a term $\phi_{\mathrm{p}}(t)$ which characterizes the pulse waveform:

$$\phi_1(t) = \omega_{\mathrm{tx}}t + \phi_{\mathrm{p}}(t). \tag{41}$$

The overall effective transmitter offset relative to the receiver reference frequency is equal to $\dot{\phi}_1(t) = \omega_{\mathrm{tx}} + \dot{\phi}_{\mathrm{p}}(t)$.

The jolting frame is the same as the interaction representation of $\hat{H}_0(t)$. When $\left[\hat{H}_0(t'), \hat{H}_0(t'')\right] = 0$ for all values of t' and t'', the propagator describing the accompanying frame transformation between two time points t_1 and t_2, $\hat{U}_0(t_2, t_1)$, is

$$\hat{U}_0(t_2, t_1) = \exp\left(-\mathrm{i}\int_{t_1}^{t_2}\hat{H}_0(t)\,\mathrm{d}t\right). \tag{42}$$

The Hamiltonian describing the evolution of the spin system in the jolting frame, denoted $\tilde{H}(t)$, is given by

$$\tilde{H}(t) = \hat{U}_0(t, 0)^{-1}\hat{H}_1(t)\hat{U}_0(t, 0). \tag{43}$$

We note that, in general, this Hamiltonian has two sources of time dependence, which are the periodic oscillation due to the modulation of the anisotropic spin interaction by MAS, and the time dependence of the pulse waveform. Hence we can write the jolting-frame Hamiltonian as [44]

$$\tilde{H}(t) = \sum_{p=-\infty}^{+\infty}\hat{h}_p(t)\exp(\mathrm{i}p\omega_{\mathrm{r}}t). \tag{44}$$

The periodic modulation due to MAS is described by the plane-wave functions, and the time dependence of the pulse is accounted for in the time-dependent coefficients $\hat{h}_p(t)$. In this frame we have a different picture of the pulse compared to that outlined above for the standard rotating frame. Now we have a spin with a static resonance frequency of zero, and the pulse transmitter

is varying periodically according to the inverse MAS modulation of the anisotropic interaction. Once again the pulse is resonant with the spin for only a fraction of the pulse length, but this is now due to the modulation of the transmitter frequency. As this modulation is periodic over τ_r we can write the Hamiltonian as in equation 44, which represents a 'comb' of RF pulses that are applied at integer multiples of the spinning frequency.

The Hamiltonian $\tilde{H}(t)$ gives an exact description of the spin dynamics in the jolting frame. However it is difficult to interpret the behaviour in a qualitative or quantitative manner due to the time dependencies from multiple sources, especially as $\left[\tilde{H}(t'), \tilde{H}(t'')\right] \neq 0$ for arbitrary t' and t''. However we can model the effect of this Hamiltonian using either the concept of effective Hamiltonians in Floquet theory [45–48], or average Hamiltonians in average Hamiltonian theory (AHT) [36, 49].

B. Non-stroboscopic observation described by Floquet theory

The idea of Floquet theory is ultimately to represent the jolting-frame Hamiltonian $\tilde{H}(t)$ as an effective Hamiltonian which takes the form of a series expansion, and which describes the evolution of the spin system at arbitrary times [45–48]. If we apply the assumption that the time dependence due to the pulse waveform occurs on a timescale that is much longer than the rotor period τ_r, which is generally the case for low-power pulses, we can use single-mode Floquet theory to treat the MAS to give the following effective Hamiltonian:

$$\tilde{H}_{\text{eff}}(t) = \sum_{r=1}^{+\infty} \tilde{H}_{\text{eff}}^{(r)}(t), \tag{45}$$

where the rth-order term $\tilde{H}_{\text{eff}}^{(r)}(t)$ is referred to as the rth-order effective Hamiltonian. The time dependence due to MAS has been removed, and so the remaining time dependence in $\tilde{H}_{\text{eff}}^{(r)}(t)$ is due solely to the modulation of the pulse amplitude and phase. This model has been used successfully to describe the effect of low-power S^3APs on spins $I = 1/2$ subject to large SA interactions, and so we use it here to model the effect of S^3APs applied to spins $I = 1$. Here we use the effective Hamiltonians up to third order to model the effect of the S^3AP. Starting from the jolting-frame Hamiltonian in equation 44 the first-, second-, and third-order effective Hamiltonians have the

following expressions [48]:

$$\tilde{H}^{(1)}_{\mathrm{eff}}(t) = \hat{h}_0(t), \tag{46}$$

$$\tilde{H}^{(2)}_{\mathrm{eff}}(t) = -\frac{1}{2}\sum_{p\neq 0}\frac{\left[\hat{h}_{-p}(t), \hat{h}_{+p}(t)\right]}{p\omega_{\mathrm{r}}}, \tag{47}$$

$$\tilde{H}^{(3)}_{\mathrm{eff}}(t) = -\frac{1}{2}\sum_{p\neq 0}\frac{\left[\left[\hat{h}_0(t), \hat{h}_{+p}(t)\right], \hat{h}_{-p}(t)\right]}{p^2\omega_{\mathrm{r}}^2} - \frac{1}{3}\sum_{p\neq 0}\sum_{p'\neq p\neq 0}\frac{\left[\left[\hat{h}_{p-p'}(t), \hat{h}_{+p'}(t)\right], \hat{h}_{-p}(t)\right]}{pp'\omega_{\mathrm{r}}^2}. \tag{48}$$

C. Stroboscopic observation described by average Hamiltonian theory

The double-quantum excitation pulse schemes that are described here employ conventional pulses of constant amplitude and phase. In this case the time dependence is due only to the MAS, and we can define an average Hamiltonian $\overline{H}$ that describes the evolution of the spin system if we restrict the observation of the density operator to time points that are integer multiples of the rotor period, referred to as stroboscopic observation. The average Hamiltonian can be calculated from the (now time-independent) effective Floquet Hamiltonian by a unitary transformation described by an operator $\hat{\Delta}$ [48]:

$$\overline{H} = \hat{\Delta}\tilde{H}_{\mathrm{eff}}\hat{\Delta}^{-1} \tag{49}$$

$$= \sum_{r=1}^{+\infty}\overline{H}^{(r)}, \tag{50}$$

where $\overline{H}^{(r)}$ is the rth-order average Hamiltonian, which is given by

$$\overline{H}^{(r)} = \hat{\Delta}\tilde{H}^{(r)}_{\mathrm{eff}}\hat{\Delta}^{-1}. \tag{51}$$

The average Hamiltonians can be calculated more simply by AHT. The first-, second-, and third-order average Hamiltonians are given by the following integral expressions [36, 49]:

$$\overline{H}^{(1)} = \frac{1}{\tau_{\mathrm{r}}}\int_0^{\tau_{\mathrm{r}}}\tilde{H}(t_1)\,\mathrm{d}t_1, \tag{52}$$

$$\overline{H}^{(2)} = -\frac{\mathrm{i}}{2\tau_{\mathrm{r}}}\int_0^{\tau_{\mathrm{r}}}\int_0^{t_2}\left[\tilde{H}(t_2), \tilde{H}(t_1)\right]\,\mathrm{d}t_1\mathrm{d}t_2, \tag{53}$$

$$\overline{H}^{(3)} = -\frac{1}{6\tau_{\mathrm{r}}}\int_0^{\tau_{\mathrm{r}}}\int_0^{t_3}\int_0^{t_2}\left\{\left[\tilde{H}(t_3), \left[\tilde{H}(t_2), \tilde{H}(t_1)\right]\right] + \left[\tilde{H}(t_1), \left[\tilde{H}(t_2), \tilde{H}(t_3)\right]\right]\right\}\,\mathrm{d}t_1\mathrm{d}t_2\mathrm{d}t_3. \tag{54}$$

Substituting in the jolting-frame Hamiltonian in equation 44, we obtain:

$$\overline{H}^{(1)} = \hat{h}_0, \tag{55}$$

$$\overline{H}^{(2)} = -\frac{1}{2}\sum_{p\neq 0}\frac{\left[\hat{h}_{-p},\hat{h}_{+p}\right]}{p\omega_{\mathrm{r}}} + \sum_{p\neq 0}\frac{\left[\hat{h}_0,\hat{h}_{+p}\right]}{p\omega_{\mathrm{r}}}, \tag{56}$$

$$\begin{aligned}\overline{H}^{(3)} =& \frac{1}{3}\sum_{p\neq 0}\sum_{p'\neq p\neq 0}\frac{\left[\hat{h}_{+p'},\left[\hat{h}_{p-p'},\hat{h}_{-p}\right]\right]}{pp'\omega_{\mathrm{r}}^2} + \frac{1}{2}\sum_{p\neq 0}\frac{\left[\hat{h}_{+p},\left[\hat{h}_0,\hat{h}_{-p}\right]\right]}{p^2\omega_{\mathrm{r}}^2} - \frac{1}{2}\sum_{p\neq 0}\frac{\left[\hat{h}_0,\left[\hat{h}_0,\hat{h}_{+p}\right]\right]}{p^2\omega_{\mathrm{r}}^2} \\ &+ \sum_{p\neq 0}\sum_{p'\neq 0}\frac{\left[\hat{h}_{+p'},\left[\hat{h}_{-p'},\hat{h}_{+p}\right]\right]}{pp'\omega_{\mathrm{r}}^2} + \frac{1}{2}\sum_{p\neq 0}\sum_{p'\neq 0}\frac{\left[\hat{h}_{+p'},\left[\hat{h}_{+p},\hat{h}_0\right]\right]}{pp'\omega_{\mathrm{r}}^2}.\end{aligned} \tag{57}$$

IV. RADIOFREQUENCY PULSE SCHEMES

We now outline the RF pulse schemes that are used in the work described here. The double-quantum excitation sequences employ conventional RF pulses with constant field amplitude and phase, whilst the low-power inversion experiments are performed using S^3APs, which are are swept-frequency adiabatic pulses. Following this we examine the conditions under which a pulse designed for inversion can be used successfully as a refocusing pulse.

A. Conventional pulses

The simplest pulse is one of constant RF field amplitude ω_1 and phase ϕ_{p}, and therefore has a time-independent waveform. The Hamiltonian $\hat{H}_1$ is also time independent, and is written immediately from equation 40 as

$$\hat{H}_1 = \omega_1 \hat{R}_z\left(\phi_{\mathrm{p}}\right)\hat{I}_x\hat{R}_z\left(\phi_{\mathrm{p}}\right)^{-1}. \tag{58}$$

The pulse is applied for a time τ_{p}, which is referred to as the pulse length. When applied to an isolated spin so that it is exactly resonant with the resonance frequency the equilibrium density operator, which is proportional to $\hat{I}_z$, undergoes the following transformation expressed in Cartesian basis operators:

$$\hat{I}_z \rightarrow \cos\left(\theta_{\mathrm{p}}\right)\hat{I}_z - \sin\left(\theta_{\mathrm{p}}\right)\cos\left(\phi_{\mathrm{p}}\right)\hat{I}_y + \sin\left(\theta_{\mathrm{p}}\right)\sin\left(\phi_{\mathrm{p}}\right)\hat{I}_x, \tag{59}$$

where $\theta_{\mathrm{p}} = \omega_1\tau_{\mathrm{p}}$ is the nominal flip angle.

B. Swept-frequency adiabatic pulses

The second class of pulse considered here is the swept-frequency adiabatic pulse, for which the amplitude and phase profiles satisfy the following conditions [5]:

$$\omega_1(t) = \omega_1(\tau_\mathrm{p} - t), \tag{60}$$

$$\phi_\mathrm{p}(t) = \phi_\mathrm{p}(\tau_\mathrm{p} - t). \tag{61}$$

The amplitude profile normally comprises a slow ramp-up of the RF field at the beginning of the pulse, and a corresponding ramp down at the end, and may have constant amplitude for the central part of the pulse waveform. The phase profile is usually more important for determining the inversion properties of the pulse. The condition imposed above ensures that the effective transmitter offset relative to the receiver reference frequency satisfies

$$\dot{\phi}_\mathrm{p}(t) = -\dot{\phi}_\mathrm{p}(\tau_\mathrm{p} - t). \tag{62}$$

Both $\phi_\mathrm{p}(t)$ and $\dot{\phi}_\mathrm{p}(t)$ are characterised by a parameter that describes the range of frequencies over which the effective transmitter sweeps during the pulse, and which determines the inversion bandwidth of the pulse. The class of adiabatic pulses considered here are the WURST-n pulses of Kupce and Freeman [11], which have been shown to be effective S^{3}APs [4, 15, 18]. The amplitude, phase, and effective transmitter-offset profiles are

$$\omega_1(t) = \omega_1^\mathrm{max}\left[1 - \left|\sin\left\{\pi\left(t/\tau_\mathrm{p} - 1/2\right)\right\}\right|^n\right], \tag{63}$$

$$\phi_\mathrm{p}(t) = \frac{\Delta\omega}{2}\left(\frac{t^2}{\tau_\mathrm{p}} - t + \frac{\tau_\mathrm{p}}{4}\right), \tag{64}$$

$$\dot{\phi}_\mathrm{p}(t) = \frac{\Delta\omega}{2}\left(\frac{2t}{\tau_\mathrm{p}} - 1\right), \tag{65}$$

where ω_1^max and $\Delta\omega$ are the peak RF field amplitude and sweep width of the pulse. The conditions for successful inversion with these pulses is discussed in detail below. It should be emphasised that, despite the emphasis here on the WURST-n pulses, the description of the S^{3}AP also applies to other adiabatic pulse waveforms, such as the hyperbolic secant [12, 14, 16, 17], and pulses with optimized sweep profiles [50]. In particular this latter class of pulse is observed to perform better than the standard WURST for short sweeps.

C. The excitation sculpting principle

We now discuss the use of RF pulse schemes in the role of refocussing pulses, rather than for inversion. Refocussing is more demanding than inversion, because for the former we simply need to convert the density operator $\hat{I}_z$ to $-\hat{I}_z$, whereas for the latter we need to convert the +1-coherence operator $\hat{I}_+$ to the −1-coherence operator $\hat{I}_-$ (and vice versa), *without introducing any frequency- or orientation-dependent phase errors*. However there is an elegant idea which enables one to use a pulse scheme designed exclusively for inversion as a successful refocussing element. This excitation sculpting principle was first developed for isotropic spin systems in solution NMR [51, 52], but can equally-well be used to describe anisotropic spin systems under MAS [4].

The description of excitation sculpting begins with a pulse sequence S, which may be a single pulse, composite pulse, or combination of pulses and delays such as a spin echo. The only condition is that the duration of the sequence τ_S must be an integer number of rotor periods. The Hamiltonian describing the density-operator evolution during S comprises both the RF term $\hat{H}_1(t)$ and the Hamiltonian describing the interactions under MAS $\hat{H}_0(t)$. Now we give an important second condition that the total Hamiltonian contains only spin terms of spherical-tensor rank one. In particular this means that $\hat{H}_0(t)$ contains only interactions such as the chemical shift and SA, and does not include interactions of spin rank two, such as homonuclear dipolar couplings or, more importantly for $I = 1$, quadrupolar interactions. If only rank-one interactions are present we can describe the overall effect of the pulse sequence on the spin system via the following propagator, which represents a rotation about an axis in spin space as specified by a set of Euler angles $\Omega_S = (\alpha_S, \beta_S, \gamma_S)$:

$$\hat{U}(\alpha_\mathrm{S}, \beta_\mathrm{S}, \gamma_\mathrm{S}) = \hat{R}_z(\alpha_\mathrm{S})\,\hat{R}_y(\beta_\mathrm{S})\,\hat{R}_z(\gamma_\mathrm{S})\,. \tag{66}$$

We note that Ω_S contains information about the system Hamiltonian under MAS in addition to the RF irradiation. The transformation of the density operator can now be computed using the well-known transformation rules governing rotations of irreducible spherical-tensor operators [53].

To describe inversion we apply the propagator to the density operator which represents the spin system at thermal equilibrium, which in spherical-tensor notation is $\hat{\rho}_0 = \hat{T}_{10}$. The pulse sequence

causes the following transformation:

$$\hat{\rho}_1 = \hat{U}(\alpha_S, \beta_S, \gamma_S)\,\hat{T}_{10}\hat{U}(\alpha_S, \beta_S, \gamma_S)^{-1} \tag{67}$$

$$= d^{(1)}_{00}(\beta_S)\,\hat{T}_{10} \tag{68}$$

$$= \cos(\beta_S)\,\hat{T}_{10}, \tag{69}$$

where we have retained only the term in $\hat{T}_{10}$. The extent of inversion is given by the factor $\cos(\beta_S)$, with complete inversion being achieved when $\beta_S = \pi$. To describe refocussing we set the initial density operator to $\hat{\rho}_0 = \hat{T}_{1-1}$. Following the sequence S, and phase-cycling to retain only the term in $\hat{T}_{1+1}$, so that the coherence order has changed from -1 to $+1$, we obtain the following:

$$\hat{\rho}_1 = \hat{U}(\alpha_S, \beta_S, \gamma_S)\,\hat{T}_{1-1}\hat{U}(\alpha_S, \beta_S, \gamma_S)^{-1} \tag{70}$$

$$= d^{(1)}_{+1-1}(\beta_S)\exp(-\mathrm{i}(\alpha_S - \gamma_S))\,\hat{T}_{1+1} \tag{71}$$

$$= \frac{1}{2}(1 - \cos(\beta_S))\exp(-\mathrm{i}(\alpha_S - \gamma_S))\,\hat{T}_{1+1}. \tag{72}$$

The amplitude of $\hat{\rho}_1$, $(1 - \cos(\beta_S))/2$, depends on the β_S, and is at the maximum possible value when $\beta_S = \pi$, i.e. the condition for complete inversion. However the density operator also acquires a phase $-\alpha_S + \gamma_S$, which depends not only on the details of the RF pulse but also on the spin-system interaction parameters, crystallite orientation, and MAS frequency. This phase error renders the sequence S as unsuitable for refocussing. The solution is to apply S for a second time, with the difference that we select the opposite change of coherence order from $+1$ to -1, to give the density operator $\hat{\rho}_2$. Retaining only the term with coherence order -1, represented by $\hat{T}_{1-1}$, the result is

$$\hat{\rho}_2 = d^{(1)}_{+1-1}(\beta_S)\exp(-\mathrm{i}(\alpha_S - \gamma_S))\,\hat{U}(\alpha_S, \beta_S, \gamma_S)\,\hat{T}_{1+1}\hat{U}(\alpha_S, \beta_S, \gamma_S)^{-1} \tag{73}$$

$$= d^{(1)}_{+1-1}(\beta_S)\,d^{(1)}_{-1+1}(\beta_S)\exp(-\mathrm{i}(\alpha_S - \gamma_S))\exp(+\mathrm{i}(\alpha_S - \gamma_S))\,\hat{T}_{1-1} \tag{74}$$

$$= \frac{1}{4}(1 - \cos(\beta_S))^2\,\hat{T}_{1-1}. \tag{75}$$

We see that the two phase errors have cancelled, leaving an overall phase of zero, and that the amplitude is now the square of $(1 - \cos(\beta_S))/2$. We obtain the maximum signal intensity of unity if $\beta_S = \pi$, and so we see that we can use any pulse sequence designed for inversion as a refocusing element if we employ the sequence twice.

As noted above the excitation sculpting principle applies only if we have spin-rank-one terms in the Hamiltonian, and so we would expect the refocussing efficiency to break down if we introduce non-negligible rank-two interactions such as the first-order quadrupole interaction.

V. THE THEORETICAL DESCRIPTION OF PULSE SCHEMES FOR BROADBAND INVERSION OF A SPIN $I = 1$ IN PRESENCE OF FIRST-ORDER QUADRUPOLAR INTERACTION

Here we extend the theory of the S^{3}AP to describe the adiabatic inversion of a spin $I = 1$ that is subject to a large first-order quadrupole interaction. Whilst the logic behind the idea is the same as for the case of the SA discussed discussed in ref. [18], the results are somewhat more complex due to the different form of the spin interaction. For comparison the results for a spin $I = 1$ experiencing a large SA are summarised in the SI. The theoretical formalism developed in this section allows us for the first time to obtain complete experimental ^{14}N population inversion using low-power RF irradiation.

A. The jolting-frame description

The propagator $\hat{U}_0(t_2, t_1)$, which describes the transformation from the rotating frame to the jolting frame in equation 43, is the propagator $\hat{U}_\mathrm{q}^\mathrm{Q}(\gamma_\mathrm{QR}; t_2, t_1)$ which describes evolution under the first-order quadrupolar Hamiltonian $\hat{H}_\mathrm{q}^\mathrm{Q}(\gamma_\mathrm{QR}; t)$. This propagator is

$$\hat{U}_\mathrm{q}^\mathrm{Q}(\gamma_\mathrm{QR}; t_2, t_1) = \exp\left(-\mathrm{i}\int_{t_1}^{t_2} \hat{H}_\mathrm{q}^\mathrm{Q}(\gamma_\mathrm{QR}; t)\,\mathrm{d}t\right). \tag{76}$$

The propagator commutes with the spin operator $\hat{I}_z$, and so we can write the jolting-frame Hamiltonian as

$$\tilde{H}(t) = \omega_1(t)\hat{R}_z\left(\phi_1(t)\right)\hat{U}_\mathrm{q}^\mathrm{Q}(\gamma_\mathrm{QR}; t, 0)^{-1}\hat{I}_x\hat{U}_\mathrm{q}^\mathrm{Q}(\gamma_\mathrm{QR}; t, 0)\hat{R}_z\left(\phi_1(t)\right)^{-1}, \tag{77}$$

where the pulse phase $\phi_1(t) = n\omega_\mathrm{r}t + \phi_\mathrm{p}(t)$ describes an S^{3}AP which simultaneously sweeps through the nth-order sideband of the transition $|+1\rangle \rightarrow |0\rangle$ (of intensity $B_\mathrm{q}^{(n)}$ and phase $\xi_\mathrm{q}^{(n)}(\gamma_\mathrm{QR})$), and the nth-order sideband of the transition $|0\rangle \rightarrow |-1\rangle$ (of intensity $B_\mathrm{q}^{(-n)}$ and phase $-\xi_\mathrm{q}^{(-n)}(\gamma_\mathrm{QR})$). The transformation of the spin operator $\hat{I}_x$ under the forward propagator $\hat{U}_\mathrm{q}^\mathrm{Q}(\gamma_\mathrm{QR}; t, 0)$ is described in

the SI:

$$\hat{I}_x = \sqrt{2}\hat{I}_x^{(+1,0)} + \sqrt{2}\hat{I}_x^{(0,-1)} \tag{78}$$

$$\rightarrow \sqrt{2}\left[\hat{I}_x^{(+1,0)}\cos\left[\Phi_{\mathrm{q}}^{\mathrm{Q}}(\gamma_{\mathrm{QR}};t,0)\right] + \hat{I}_y^{(+1,0)}\sin\left[\Phi_{\mathrm{q}}^{\mathrm{Q}}(\gamma_{\mathrm{QR}};t,0)\right]\right]$$

$$+ \sqrt{2}\left[\hat{I}_x^{(0,-1)}\cos\left[\Phi_{\mathrm{q}}^{\mathrm{Q}}(\gamma_{\mathrm{QR}};t,0)\right] - \hat{I}_y^{(0,-1)}\sin\left[\Phi_{\mathrm{q}}^{\mathrm{Q}}(\gamma_{\mathrm{QR}};t,0)\right]\right] \tag{79}$$

$$= \sqrt{2}\hat{R}_z^{(+1,0)}\left(\Phi_{\mathrm{q}}^{\mathrm{Q}}(\gamma_{\mathrm{QR}};t,0)\right)\hat{I}_x^{(+1,0)}\hat{R}_z^{(+1,0)}\left(\Phi_{\mathrm{q}}^{\mathrm{Q}}(\gamma_{\mathrm{QR}};t,0)\right)^{-1}$$

$$+ \sqrt{2}\hat{R}_z^{(0,-1)}\left(-\Phi_{\mathrm{q}}^{\mathrm{Q}}(\gamma_{\mathrm{QR}};t,0)\right)\hat{I}_x^{(0,-1)}\hat{R}_z^{(0,-1)}\left(-\Phi_{\mathrm{q}}^{\mathrm{Q}}(\gamma_{\mathrm{QR}};t,0)\right)^{-1}, \tag{80}$$

where the rotation operators are defined as

$$\hat{R}_a^{(M_1,M_2)}(\phi) = \exp\left(-\mathrm{i}\phi\hat{I}_a^{(M_1,M_2)}\right). \tag{81}$$

We see that $\hat{I}_x$ splits into the x-spin operators for the two single-quantum transitions, $\hat{I}_x^{(+1,0)}$ and $\hat{I}_x^{(0,-1)}$, which evolve at the same frequency, but in opposite directions about their respective z-axes. Applying the inverse of this transformation, and expanding the phase factors of $\Phi_{\mathrm{q}}^{\mathrm{Q}}(\gamma_{\mathrm{QR}};t,0)$ as Fourier series we obtain the following jolting-frame Hamiltonian:

$$\tilde{H}(t) = \sqrt{2}\omega_1(t)\sum_{m=-\infty}^{+\infty}\Bigg[B_{\mathrm{q}}^{(m)}\hat{R}_z^{(+1,0)}\left(\phi_{\mathrm{p}}(t) - \xi_{\mathrm{q}}^{(m)}(\gamma_{\mathrm{QR}}) + (n-m)\omega_{\mathrm{r}}t\right)\hat{I}_x^{(+1,0)}\hat{R}_z^{(+1,0)}\left(\phi_{\mathrm{p}}(t) - \xi_{\mathrm{q}}^{(m)}(\gamma_{\mathrm{QR}}) + (n-m)\omega_{\mathrm{r}}t\right)^{-1}$$

$$+ B_{\mathrm{q}}^{(m)}\hat{R}_z^{(0,-1)}\left(\phi_{\mathrm{p}}(t) + \xi_{\mathrm{q}}^{(m)}(\gamma_{\mathrm{QR}}) + (n+m)\omega_{\mathrm{r}}t\right)\hat{I}_x^{(0,-1)}\hat{R}_z^{(0,-1)}\left(\phi_{\mathrm{p}}(t) + \xi_{\mathrm{q}}^{(m)}(\gamma_{\mathrm{QR}}) + (n+m)\omega_{\mathrm{r}}t\right)^{-1}\Bigg]. \tag{82}$$

At first glance this Hamiltonian has a rather complex appearance. However it can be understood in a relatively straightforward manner.

The jolting frame Hamiltonian comprises two combs of RF pulses, each applied to one of the single-quantum transitions. The comb that is applied to the transition $|+1\rangle \rightarrow |0\rangle$ comprises a series of pulses m with effective transmitter frequencies $(n-m)\omega_{\mathrm{r}}$, RF field amplitudes $\sqrt{2}\omega_1(t)B_{\mathrm{q}}^{(m)}$, and constant phases $-\xi_{\mathrm{q}}^{(m)}(\gamma_{\mathrm{QR}})$ relative to the pulse phase. The second comb applied to the other transition $|0\rangle \rightarrow |-1\rangle$ comprises a series of pulses with the same effective transmitter offsets $(n-m)\omega_{\mathrm{r}}$, RF field amplitudes $\sqrt{2}\omega_1(t)B_{\mathrm{q}}^{(-m)}$, and phases $+\xi_{\mathrm{q}}^{(-m)}(\gamma_{\mathrm{QR}})$. The sign change in m associated with the second transition is a consequence of the spinning sideband manifold of the second transition being a related to the first by a reversal of the frequency axis.

We now rewrite the jolting-frame Hamiltonian in the form of equation 44 using the following steps. Firstly we change the summation index from m to p, by setting $p = n - m$ in the terms involving the transition $|+1\rangle \rightarrow |0\rangle$, and $p = n + m$ in the terms involving the transition $|0\rangle \rightarrow |-1\rangle$:

$$\tilde{H}(t) = \sqrt{2}\omega_1(t) \sum_{p=-\infty}^{+\infty} \Big[B_{\mathrm{q}}^{(n-p)} \hat{R}_z^{(+1,0)} \left(\phi_{\mathrm{p}}(t) - \xi_{\mathrm{q}}^{(n-p)}(\gamma_{\mathrm{QR}}) + p\omega_{\mathrm{r}}t\right) \hat{I}_x^{(+1,0)} \hat{R}_z^{(+1,0)} \left(\phi_{\mathrm{p}}(t) - \xi_{\mathrm{q}}^{(n-p)}(\gamma_{\mathrm{QR}}) + p\omega_{\mathrm{r}}t\right)^{-1} + B_{\mathrm{q}}^{(-n+p)} \hat{R}_z^{(0,-1)} \left(\phi_{\mathrm{p}}(t) + \xi_{\mathrm{q}}^{(-n+p)}(\gamma_{\mathrm{QR}}) + p\omega_{\mathrm{r}}t\right) \hat{I}_x^{(0,-1)} \hat{R}_z^{(0,-1)} \left(\phi_{\mathrm{p}}(t) + \xi_{\mathrm{q}}^{(-n+p)}(\gamma_{\mathrm{QR}}) + p\omega_{\mathrm{r}}t\right)^{-1} \Big]. \tag{83}$$

Secondly we rewrite the Cartesian spin operators in terms of the fictitious spin-1/2 raising and lowering operators $\hat{I}_{\pm}^{(M_1,M_2)}$, which are defined as

$$\hat{I}_{\pm}^{(M_1,M_2)} = \hat{I}_x^{(M_1,M_2)} \pm \mathrm{i}\hat{I}_y^{(M_1,M_2)}, \tag{84}$$

and apply the following expressions for the z-rotations of $\hat{I}_{\pm}^{(M_1,M_2)}$:

$$\hat{R}_z^{(M_1,M_2)}(\phi)\hat{I}_{\pm}^{(M_1,M_2)}\hat{R}_z^{(M_1,M_2)}(\phi)^{-1} = \hat{I}_{\pm}^{(M_1,M_2)} \exp(\mp\mathrm{i}\phi). \tag{85}$$

The result is a jolting-frame Hamiltonian written in the form of equation 44:

$$\begin{aligned} \tilde{H}(t) = \sqrt{\frac{1}{2}}\omega_1(t) \sum_p \Big[& B_{\mathrm{q}}^{(n-p)} \exp\left(+\mathrm{i}\left(\phi_{\mathrm{p}}(t) - \xi_{\mathrm{q}}^{(n-p)}(\gamma_{\mathrm{QR}}) + p\omega_{\mathrm{r}}t\right)\right) \hat{I}_-^{(+1,0)} \\ & + B_{\mathrm{q}}^{(n-p)} \exp\left(-\mathrm{i}\left(\phi_{\mathrm{p}}(t) - \xi_{\mathrm{q}}^{(n-p)}(\gamma_{\mathrm{QR}}) + p\omega_{\mathrm{r}}t\right)\right) \hat{I}_+^{(+1,0)} \\ & + B_{\mathrm{q}}^{(-n+p)} \exp\left(+\mathrm{i}\left(\phi_{\mathrm{p}}(t) + \xi_{\mathrm{q}}^{(-n+p)}(\gamma_{\mathrm{QR}}) + p\omega_{\mathrm{r}}t\right)\right) \hat{I}_-^{(0,-1)} \\ & + B_{\mathrm{q}}^{(-n+p)} \exp\left(-\mathrm{i}\left(\phi_{\mathrm{p}}(t) + \xi_{\mathrm{q}}^{(-n+p)}(\gamma_{\mathrm{QR}}) + p\omega_{\mathrm{r}}t\right)\right) \hat{I}_+^{(0,-1)} \Big], \end{aligned} \tag{86}$$

in which the operator coefficients $\hat{h}_p$ are

$$\begin{aligned} \hat{h}_p(t) = \sqrt{\frac{1}{2}}\omega_1(t) \Big[& B_{\mathrm{q}}^{(n-p)} \exp\left(+\mathrm{i}\left(\phi_{\mathrm{p}}(t) - \xi_{\mathrm{q}}^{(n-p)}(\gamma_{\mathrm{QR}})\right)\right) \hat{I}_-^{(+1,0)} + B_{\mathrm{q}}^{(n+p)} \exp\left(-\mathrm{i}\left(\phi_{\mathrm{p}}(t) - \xi_{\mathrm{q}}^{(n+p)}(\gamma_{\mathrm{QR}})\right)\right) \hat{I}_+^{(+1,0)} \\ & + B_{\mathrm{q}}^{(-n+p)} \exp\left(+\mathrm{i}\left(\phi_{\mathrm{p}}(t) + \xi_{\mathrm{q}}^{(-n+p)}(\gamma_{\mathrm{QR}})\right)\right) \hat{I}_-^{(0,-1)} + B_{\mathrm{q}}^{(-n-p)} \exp\left(-\mathrm{i}\left(\phi_{\mathrm{p}}(t) + \xi_{\mathrm{q}}^{(-n-p)}(\gamma_{\mathrm{QR}})\right)\right) \hat{I}_+^{(0,-1)} \Big]. \end{aligned} \tag{87}$$

We now calculate the effective Floquet Hamiltonian. It turns out that we capture the important

features of the S^3AP applied to a quadrupole if we restrict the calculation up to second order.

The first-order effective Hamiltonian is

$$\tilde{H}^{(1)}_{\text{eff}}(t) = \sqrt{2}\omega_1(t)\Big[B^{(n)}_{\text{q}}\hat{R}^{(+1,0)}_z\left(\phi_{\text{p}}(t) - \xi^{(n)}_{\text{q}}(\gamma_{\text{QR}})\right)\hat{I}^{(+1,0)}_x\hat{R}^{(+1,0)}_z\left(\phi_{\text{p}}(t) - \xi^{(n)}_{\text{q}}(\gamma_{\text{QR}})\right)^{-1} + B^{(-n)}_{\text{q}}\hat{R}^{(0,-1)}_z\left(\phi_{\text{p}}(t) + \xi^{(-n)}_{\text{q}}(\gamma_{\text{QR}})\right)\hat{I}^{(0,-1)}_x\hat{R}^{(0,-1)}_z\left(\phi_{\text{p}}(t) + \xi^{(-n)}_{\text{q}}(\gamma_{\text{QR}})\right)^{-1}\Big]. \tag{88}$$

It comprises two single-quantum-selective RF fields, each of which is applied to one of the two single-quantum transitions. The first term is an RF field applied to the $|+1\rangle \rightarrow |0\rangle$ with amplitude $\sqrt{2}\omega_1(t)B^{(n)}_{\text{q}}$ and phase $\phi_{\text{p}}(t) - \xi^{(n)}_{\text{q}}(\gamma_{\text{QR}})$, i.e. the amplitude is scaled by the intensity of the irradiated nth-order sideband of this transition, and the phase is offset by minus the sideband phase. The second term is applied to the other transition $|0\rangle \rightarrow |-1\rangle$ and has an amplitude $\sqrt{2}\omega_1(t)B^{(-n)}_{\text{q}}$ scaled down by the intensity of the irradiated nth-order sideband of this transition, and phase $\phi_{\text{p}}(t) + \xi^{(-n)}_{\text{q}}(\gamma_{\text{QR}})$ which is offset by minus the corresponding sideband phase of this transition. The form of this Hamiltonian can be compared with the first-order effective Hamiltonian computed for an SA, given in the SI. In both cases there are two RF fields, each applied to one of the two distinct single-quantum transitions. In the case of the quadrupolar interaction the additional complexity compared to the SA is due to the former transforming $\hat{I}^{(+1,0)}_x$ and $\hat{I}^{(0,-1)}_x$ differently, whereas they are indistinguishable under the SA.

The second-order effective Hamiltonian has a more complex form than for the case of the SA given in the SI. It comprises terms proportional to the longitudinal operators for the two single-quantum transitions, $\hat{I}^{(+1,0)}_z$ and $\hat{I}^{(0,-1)}_z$, and additional double-quantum transverse terms represented by the operators $\hat{I}^{(+1,-1)}_x$ and $\hat{I}^{(+1,-1)}_y$:

$$\begin{aligned}\tilde{H}^{(2)}_{\text{eff}}(t) =& \frac{\omega_1(t)^2}{2\omega_{\text{r}}}\sum_{p\neq 0}\left\{\frac{\left(B^{(n+p)}_{\text{q}}\right)^2 - \left(B^{(n-p)}_{\text{q}}\right)^2}{p}\right\}\hat{I}^{(+1,0)}_z - \frac{\omega_1(t)^2}{2\omega_{\text{r}}}\sum_{p\neq 0}\left\{\frac{\left(B^{(-n+p)}_{\text{q}}\right)^2 - \left(B^{(-n-p)}_{\text{q}}\right)^2}{p}\right\}\hat{I}^{(0,-1)}_z \\ &+ \frac{\omega_1(t)^2}{2\omega_{\text{r}}}\sum_{p\neq 0}B^{(n+p)}_{\text{q}}B^{(-n+p)}_{\text{q}}\hat{R}^{(+1,-1)}_z\left(2\phi_{\text{p}}(t) - \xi^{(n+p)}_{\text{q}}(\gamma_{\text{QR}}) + \xi^{(-n+p)}_{\text{q}}(\gamma_{\text{QR}})\right) \\ &\times \hat{I}^{(+1,-1)}_x\hat{R}^{(+1,-1)}_z\left(2\phi_{\text{p}}(t) - \xi^{(n+p)}_{\text{q}}(\gamma_{\text{QR}}) + \xi^{(-n+p)}_{\text{q}}(\gamma_{\text{QR}})\right)^{-1} \\ &- \frac{\omega_1(t)^2}{2\omega_{\text{r}}}\sum_{p\neq 0}B^{(n-p)}_{\text{q}}B^{(-n-p)}_{\text{q}}\hat{R}^{(+1,-1)}_z\left(2\phi_{\text{p}}(t) - \xi^{(n-p)}_{\text{q}}(\gamma_{\text{QR}}) + \xi^{(-n-p)}_{\text{q}}(\gamma_{\text{QR}})\right) \\ &\times \hat{I}^{(+1,-1)}_x\hat{R}^{(+1,-1)}_z\left(2\phi_{\text{p}}(t) - \xi^{(n-p)}_{\text{q}}(\gamma_{\text{QR}}) + \xi^{(-n-p)}_{\text{q}}(\gamma_{\text{QR}})\right)^{-1}.\end{aligned} \tag{89}$$

The two longitudinal spin terms have the same form as, and are an analogy to, the second-order effective Hamiltonian calculated under the SA interaction (see SI). The double-quantum terms are, however, a new feature that arises from the different transformations of $\hat{I}_x^{(+1,0)}$ and $\hat{I}_x^{(0,-1)}$ under the quadrupolar interaction.

The expressions are relatively complicated. However the essential features of the S^{3}AP can be described by examining the special case in which we irradiate the centreband $n = 0$. Since we are now irradiating the same sideband of both transitions the effective Hamiltonians have a simpler form which we use henceforth. However it should be borne in mind that the description given in this case essentially also applies to an S^{3}AP that irradiates the other sidebands, although the mathematical details are more complicated. On irradiating the centreband the first-order effective Hamiltonian becomes

$$\begin{aligned}\tilde{H}_{\text{eff}}^{(1)}(t) = \sqrt{2}\omega_1(t)B_{\text{q}}^{(0)}\Big[&\hat{R}_z^{(+1,0)}\left(\phi_{\text{p}}(t) - \xi_{\text{q}}^{(0)}(\gamma_{\text{QR}})\right)\hat{I}_x^{(+1,0)}\hat{R}_z^{(+1,0)}\left(\phi_{\text{p}}(t) - \xi_{\text{q}}^{(0)}(\gamma_{\text{QR}})\right)^{-1} \\ &+ \hat{R}_z^{(0,-1)}\left(\phi_{\text{p}}(t) + \xi_{\text{q}}^{(0)}(\gamma_{\text{QR}})\right)\hat{I}_x^{(0,-1)}\hat{R}_z^{(0,-1)}\left(\phi_{\text{p}}(t) + \xi_{\text{q}}^{(0)}(\gamma_{\text{QR}})\right)^{-1}\Big] \qquad (90)\\ =&\omega_1(t)B_{\text{q}}^{(0)}\hat{R}_z\left(\phi_{\text{p}}(t)\right)\hat{U}_{\text{q}}^{\text{Q}}\left(\xi_{\text{q}}^{(0)}\right)^{-1}\hat{I}_x\hat{U}_{\text{q}}^{\text{Q}}\left(\xi_{\text{q}}^{(0)}\right)\hat{R}_z\left(\phi_{\text{p}}(t)\right)^{-1}, \qquad (91)\end{aligned}$$

where the quadrupolar propagator $\hat{U}_{\text{q}}^{\text{Q}}(\phi)$ is defined as

$$\hat{U}_{\text{q}}^{\text{Q}}(\phi) = \exp\left[-\text{i}\phi\left(\hat{I}_z^2 - \frac{1}{3}I(I+1)\hat{E}\right)\right]. \qquad (92)$$

Likewise the second-order effective Hamiltonian also has a considerably simplified form, which is

$$\begin{aligned}\tilde{H}_{\text{eff}}^{(2)}(t) &= \frac{\omega_1(t)^2}{2\omega_{\text{r}}}c_\Sigma\left[\hat{I}_z^{(+1,0)} - \hat{I}_z^{(0,-1)} + \hat{R}_z^{(+1,-1)}\left(2\phi_{\text{p}}(t)\right)\hat{I}_x^{(+1,-1)}\hat{R}_z^{(+1,-1)}\left(2\phi_{\text{p}}(t)\right)^{-1}\right] \qquad (93)\\ &= \frac{\omega_1(t)^2}{2\omega_{\text{r}}}c_\Sigma\left[\hat{I}_z^{(+1,0)} - \hat{I}_z^{(0,-1)} + \hat{R}_z\left(\phi_{\text{p}}(t)\right)\hat{I}_x^{(+1,-1)}\hat{R}_z\left(\phi_{\text{p}}(t)\right)^{-1}\right], \qquad (94)\end{aligned}$$

with the dimensionless quantity c_Σ being the following sum over all sidebands:

$$c_\Sigma = \sum_{p\neq 0}\frac{\left(B_{\text{q}}^{(+p)}\right)^2 - \left(B_{\text{q}}^{(-p)}\right)^2}{p}. \qquad (95)$$

Rewritten in terms of the irreducible spherical tensor operator basis the effective Hamiltonians are

$$\tilde{H}^{(1)}_{\text{eff}}(t) = \sqrt{\frac{1}{2}}\omega_1(t)B^{(0)}_{\text{q}}\cos\left(\xi^{(0)}_{\text{q}}\right)\left[\exp(+\text{i}\phi_{\text{p}}(t))\hat{T}_{1-1} - \exp(-\text{i}\phi_{\text{p}}(t))\hat{T}_{1+1}\right] - \text{i}\omega_1(t)B^{(0)}_{\text{q}}\sin\left(\xi^{(0)}_{\text{q}}\right)\left[\exp(+\text{i}\phi_{\text{p}}(t))\hat{T}_{2-1} + \exp(-\text{i}\phi_{\text{p}}(t))\hat{T}_{2+1}\right], \quad (96)$$

$$\tilde{H}^{(2)}_{\text{eff}}(t) = \frac{\omega_1(t)^2}{2\omega_{\text{r}}}c_\Sigma\left[\sqrt{\frac{3}{2}}\hat{T}_{20} + \frac{1}{2}\left(\exp(+2\text{i}\phi_{\text{p}}(t))\hat{T}_{2-2} + \exp(-2\text{i}\phi_{\text{p}}(t))\hat{T}_{2+2}\right)\right]. \quad (97)$$

Both Hamiltonians contain contributions from second-rank tensors, and so we would not necessarily expect the excitation sculpting principle to hold. The adiabatic inversion and refocussing properties are examined next.

B. Adiabatic inversion and refocussing

We now examine the adiabatic inversion and refocussing properties of an S^3AP applied to a spin $I = 1$ under the influence of a first-order quadrupolar interaction. As the effective Hamiltonians in the jolting frame are more complicated than for a spin subject to an SA [18] (see SI), so are the mathematics underpinning the spin dynamics due to the pulse. The effect of this pulse on the spin system is more easily analysed following a transformation into a superadiabatic reference frame [4, 54]. In the first step we transform the effective Floquet Hamiltonians in equations 91 and 94 from the jolting frame to a frequency-modulated frame with the transformation propagator $\hat{R}_z\left(\phi_{\text{p}}(t)\right)\hat{U}^{\text{Q}}_{\text{q}}\left(\xi^{(0)}_{\text{q}}\right)^{-1}$. We note that both factors in the propagator commute with each other, and that $\hat{U}^{\text{Q}}_{\text{q}}\left(\xi^{(0)}_{\text{q}}\right)$ also commutes with $\hat{I}_z^{(+1,0)} - \hat{I}_z^{(0,-1)}$, $\hat{I}_x^{(+1,-1)}$, and $\hat{I}_y^{(+1,-1)}$. The frequency-modulated Hamiltonian $\hat{H}^{(0)}(t)$ is therefore:

$$\hat{H}^{(0)}(t) = -\dot{\phi}_{\text{p}}(t)\hat{I}_z + \hat{R}_z\left(\phi_{\text{p}}(t)\right)^{-1}\hat{U}^{\text{Q}}_{\text{q}}\left(\xi^{(0)}_{\text{q}}\right)\left(\tilde{H}^{(1)}_{\text{eff}}(t) + \tilde{H}^{(2)}_{\text{eff}}(t)\right)\hat{U}^{\text{Q}}_{\text{q}}\left(\xi^{(0)}_{\text{q}}\right)^{-1}\hat{R}_z\left(\phi_{\text{p}}(t)\right) \quad (98)$$

$$= -\dot{\phi}_{\text{p}}(t)\hat{I}_z + \omega_1(t)B^{(0)}_{\text{q}}\hat{I}_x + \frac{\omega_1(t)^2}{2\omega_{\text{r}}}c_\Sigma\left[\hat{I}_z^{(+1,0)} - \hat{I}_z^{(0,-1)} + \hat{I}_x^{(+1,-1)}\right], \quad (99)$$

where the first term in $\hat{I}_z$ is a fictitious field due to the relative motions of the jolting and frequency-modulated reference frames. In order to proceed further we define two different RF-field amplitude regimes which would be relevant for different crystallite orientations under different experimental conditions (MAS frequency, RF field amplitude). We refer to these as the 'lower-power' regime

A, and 'higher-power' regime B, which are defined formally as:

$$\omega_1(t)B_{\mathrm{q}}^{(0)} \gg \frac{\omega_1(t)^2}{2\omega_{\mathrm{r}}}\left|c_\Sigma\right|, \qquad \text{regime A,} \tag{100}$$

$$\omega_1(t)B_{\mathrm{q}}^{(0)} \ll \frac{\omega_1(t)^2}{2\omega_{\mathrm{r}}}\left|c_\Sigma\right|, \qquad \text{regime B.} \tag{101}$$

In general terms, regime A applies at lower RF field amplitudes where the first-order effective Hamiltonian dominates, and regime B applies at higher RF field amplitudes where the second-order effective Hamiltonian dominates. The exact RF field amplitude at which we move from one regime to the other is $\omega_1^{\max} = \left(2B_{\mathrm{q}}^{(0)}/\left|c_\Sigma\right|\right)\omega_{\mathrm{r}}$. In practice for a powder sample under given experimental conditions this point is generally difficult to specify as it depends on the relative sizes of $B_{\mathrm{q}}^{(0)}$ and c_Σ, and therefore on the quadrupolar interaction parameters and the crystallite orientation, in addition to the MAS frequency. One may therefore find that, for a given set of experimental parameters, one crystallite may be in regime A and another may be in regime B. For each regime we have a different Hamiltonian in the frequency-modulated frame, which are denoted $\hat{H}_{\mathrm{A}}^{(0)}(t)$ and $\hat{H}_{\mathrm{B}}^{(0)}(t)$:

$$\hat{H}_{\mathrm{A}}^{(0)}(t) \approx -\dot{\phi}_{\mathrm{p}}(t)\hat{I}_z + \omega_1(t)B_{\mathrm{q}}^{(0)}\hat{I}_x, \tag{102}$$

$$\hat{H}_{\mathrm{B}}^{(0)}(t) \approx -\dot{\phi}_{\mathrm{p}}(t)\hat{I}_z + \frac{\omega_1(t)^2}{2\omega_{\mathrm{r}}}c_\Sigma\left[\hat{I}_z^{(+1,0)} - \hat{I}_z^{(0,-1)} + \hat{I}_x^{(+1,-1)}\right]. \tag{103}$$

We consider each case in turn.

We first consider the pulse operating in regime A, in which we can write the frequency-modulated Hamiltonian in terms of an effective field $\omega_{\mathrm{eff,A}}^{(0)}(t)$ and tilt angle $\theta_{\mathrm{A}}^{(0)}(t)$ as follows:

$$\hat{H}_{\mathrm{A}}^{(0)}(t) = \omega_{\mathrm{eff,A}}^{(0)}(t)\hat{R}_y\left(\theta_{\mathrm{A}}^{(0)}(t)\right)\hat{I}_z\hat{R}_y\left(\theta_{\mathrm{A}}^{(0)}(t)\right)^{-1}, \tag{104}$$

$$\omega_{\mathrm{eff,A}}^{(0)}(t)^2 = \dot{\phi}_{\mathrm{p}}(t)^2 + \left(\omega_1(t)B_{\mathrm{q}}^{(0)}\right)^2, \tag{105}$$

$$\tan\left(\theta_{\mathrm{A}}^{(0)}(t)\right) = -\frac{\omega_1(t)B_{\mathrm{q}}^{(0)}}{\dot{\phi}_{\mathrm{p}}(t)}. \tag{106}$$

We now transform into the first adiabatic frame defined by the propagator $\hat{R}_y\left(\theta_{\mathrm{A}}^{(0)}(t)\right)$ to give the Hamiltonian $\hat{H}_{\mathrm{A}}^{(1)}(t)$, which has the same form as the corresponding Hamiltonian describing the

S^3AP under the SA interaction (see SI):

$$\hat{H}_{\mathrm{A}}^{(1)}(t) = \hat{R}_y\left(\theta_{\mathrm{A}}^{(0)}(t)\right)^{-1} \hat{H}_{\mathrm{A}}^{(0)}(t)\hat{R}_y\left(\theta_{\mathrm{A}}^{(0)}(t)\right) - \dot{\theta}_{\mathrm{A}}^{(0)}(t)\hat{I}_y \tag{107}$$

$$= \omega_{\mathrm{eff,A}}^{(0)}(t)\hat{I}_z - \dot{\theta}_{\mathrm{A}}^{(0)}(t)\hat{I}_y, \tag{108}$$

where the term in $\hat{I}_y$ is the fictitious field due to the relative motions of the frequency-modulated and first-adiabatic frames. We can now define an adiabaticity factor $Q_{\mathrm{A}}^{(1)}$ as

$$\frac{1}{Q_{\mathrm{A}}^{(1)}} = \max\left|\frac{\dot{\theta}_{\mathrm{A}}^{(0)}(t)}{\omega_{\mathrm{eff,A}}^{(0)}(t)}\right|. \tag{109}$$

When the condition $Q_{\mathrm{A}}^{(1)} \gg 1$ is satisfied the pulse is adiabatic and we approximate $\hat{H}_{\mathrm{A}}^{(1)}(t)$ as

$$\hat{H}_{\mathrm{A}}^{(1)}(t) \approx \omega_{\mathrm{eff,A}}^{(0)}(t)\hat{I}_z, \tag{110}$$

which contains only the effective field along z. In this case the pulse acts in the same way as a pulse applied to a spin $I = 1$ subject to an SA and no quadrupolar interaction, and we can analyse the inversion and refocussing performance in the same way.

The overall propagator $\hat{U}_{\mathrm{A}}(t, 0)$ that describes the spin dynamics of the S^3AP in the jolting frame, and comprising the transformation from the jolting frame to the first adiabatic frame at $t = 0$, evolution under the Hamiltonian in equation 110 up to time t, and transformation back into the jolting frame at time t, is

$$\hat{U}_{\mathrm{A}}(t,0) = \hat{R}_z\left(\phi_{\mathrm{p}}(t)\right)\hat{U}_{\mathrm{q}}^{\mathrm{Q}}\left(\xi_{\mathrm{q}}^{(0)}\right)^{-1}\hat{R}_y\left(\theta_{\mathrm{A}}^{(0)}(t)\right)\hat{R}_z\left(\int_0^t \omega_{\mathrm{eff,A}}^{(0)}(t')\mathrm{d}t'\right)\hat{U}_{\mathrm{q}}^{\mathrm{Q}}\left(\xi_{\mathrm{q}}^{(0)}\right)\hat{R}_z\left(\phi_{\mathrm{p}}(0)\right)^{-1}, \tag{111}$$

where we have noted that $\theta_{\mathrm{A}}^{(0)}(0) = 0$. The inversion performance is evaluated by applying this propagator to $\hat{I}_z$, which results in the following density operator at time t:

$$\hat{\rho}(t) = \cos\left(\theta_{\mathrm{A}}^{(0)}(t)\right)\hat{I}_z + \sqrt{2}\sin\left(\theta_{\mathrm{A}}^{(0)}(t)\right)\Big[\cos\left(\phi_{\mathrm{p}}(t) - \xi_{\mathrm{q}}^{(0)}\right)\hat{I}_x^{(+1,0)} + \sin\left(\phi_{\mathrm{p}}(t) - \xi_{\mathrm{q}}^{(0)}\right)\hat{I}_y^{(+1,0)}$$
$$+ \cos\left(\phi_{\mathrm{p}}(t) + \xi_{\mathrm{q}}^{(0)}\right)\hat{I}_x^{(0,-1)} + \sin\left(\phi_{\mathrm{p}}(t) + \xi_{\mathrm{q}}^{(0)}\right)\hat{I}_y^{(0,-1)}\Big]. \tag{112}$$

At the end of the pulse $t = \tau_{\mathrm{p}}$, the tilt angle is $\theta_{\mathrm{A}}^{(0)}(\tau_{\mathrm{p}}) = \pi$, and we have obtained full inversion with $\hat{\rho}(\tau_{\mathrm{p}}) = -\hat{I}_z$. To evaluate the refocussing performance we apply the propagator to $\hat{I}_-$. On doing so

we obtain the following density operator at end of the pulse:

$$\hat{\rho}(\tau_{\mathrm{p}}) = \hat{I}_{+} \exp\left[\mathrm{i}\left\{\int_{0}^{\tau_{\mathrm{p}}} \omega_{\mathrm{eff,A}}^{(0)}(t)\mathrm{d}t - \phi_{\mathrm{p}}(0) - \phi_{\mathrm{p}}(\tau_{\mathrm{p}}) + \pi\right\}\right]. \tag{113}$$

As the pulse delivers complete inversion, we have obtained complete conversion to $\hat{I}_{+}$, but with an orientation-dependent phase. However following the excitation sculpting principle, if we apply the propagator a second time we recover $\hat{I}_{-}$, with the phase errors refocussed:

$$\hat{\rho}(2\tau_{\mathrm{p}}) = \hat{I}_{-}. \tag{114}$$

Hence we see that in regime A the excitation principle is obeyed, meaning that the population inversion efficiency can be used to calculate the refocussing efficiency directly using equations 69 and 75. This is because the operators involved in the propagator in equation 111 are all of rank one, with the exception of the factor $\hat{U}_{\mathrm{q}}^{\mathrm{Q}}\left(\xi_{\mathrm{q}}^{(0)}\right)$, which is a transformation under $\hat{T}_{20}$. However as seen from the density operator following a single pulse applied to $\hat{I}_{-}$, as shown in equation 113, it is apparent that evolution under $\hat{U}_{\mathrm{q}}^{\mathrm{Q}}\left(\xi_{\mathrm{q}}^{(0)}\right)$ self-refocusses during the course of the pulse.

In regime B, the frequency-modulated Hamiltonian takes the following form $\hat{H}_{\mathrm{B}}^{(0)}(t)$:

$$\hat{H}_{\mathrm{B}}^{(0)}(t) = -2\dot{\phi}_{\mathrm{p}}(t)\hat{I}_{z}^{(+1,-1)} + \frac{\omega_{1}(t)^{2}}{2\omega_{\mathrm{r}}} c_{\Sigma}\left[\hat{I}_{z}^{(+1,0)} - \hat{I}_{z}^{(0,-1)} + \hat{I}_{x}^{(+1,-1)}\right] \tag{115}$$

$$= \omega_{\mathrm{eff,B}}^{(0)}(t)\hat{R}_{y}^{(+1,-1)}\left(\theta_{\mathrm{B}}^{(0)}(t)\right)\hat{I}_{z}^{(+1,-1)}\hat{R}_{y}^{(+1,-1)}\left(\theta_{\mathrm{B}}^{(0)}(t)\right)^{-1} + \frac{\omega_{1}(t)^{2}}{2\omega_{\mathrm{r}}} c_{\Sigma}\left[\hat{I}_{z}^{(+1,0)} - \hat{I}_{z}^{(0,-1)}\right]. \tag{116}$$

We note that $\hat{H}_{\mathrm{B}}^{(0)}(t)$ has a marked difference to $\hat{H}_{\mathrm{A}}^{(0)}(t)$. The effective field $\omega_{\mathrm{eff,B}}^{(0)}(t)$ and tilt angle $\theta_{\mathrm{B}}^{(0)}(t)$ in the expression for $\hat{H}_{\mathrm{B}}^{(0)}(t)$ are given by

$$\omega_{\mathrm{eff,B}}^{(0)}(t)^{2} = 4\dot{\phi}_{\mathrm{p}}(t)^{2} + \frac{\omega_{1}(t)^{4}}{4\omega_{\mathrm{r}}^{2}} c_{\Sigma}^{2}, \tag{117}$$

$$\tan\left(\theta_{\mathrm{B}}^{(0)}(t)\right) = -\frac{\omega_{1}(t)^{2} c_{\Sigma}}{4\dot{\phi}_{\mathrm{p}}(t)\omega_{\mathrm{r}}}. \tag{118}$$

We now transform into the first adiabatic frame via the propagator $\hat{R}_{y}^{(+1,-1)}\left(\theta_{\mathrm{B}}^{(0)}(t)\right)$. We see that the spin operator in the first term of equation 116, $\hat{R}_{y}^{(+1,-1)}\left(\theta_{\mathrm{B}}^{(0)}(t)\right)\hat{I}_{z}^{(+1,-1)}\hat{R}_{y}^{(+1,-1)}\left(\theta_{\mathrm{B}}^{(0)}(t)\right)^{-1}$, is converted into the longitudinal term $\hat{I}_{z}^{(+1,-1)}$, and that the spin operator in the second term $\hat{I}_{z}^{(+1,0)} - \hat{I}_{z}^{(0,-1)}$ is

unaffected, as it commutes with $\hat{I}_y^{(+1,-1)}$. The resulting Hamiltonian $\hat{H}_{\mathrm{B}}^{(1)}(t)$ is therefore

$$\hat{H}_{\mathrm{B}}^{(1)}(t) = \omega_{\mathrm{eff,B}}^{(0)}(t)\hat{I}_z^{(+1,-1)} + \frac{\omega_1(t)^2}{2\omega_{\mathrm{r}}} c_\Sigma \left[\hat{I}_z^{(+1,0)} - \hat{I}_z^{(0,-1)}\right] - \dot{\theta}_{\mathrm{B}}^{(0)}(t)\hat{I}_y^{(+1,-1)}, \tag{119}$$

where we note a term in $\hat{I}_y^{(+1,-1)}$ is added to account for the motion of the adiabatic frame in the frequency-modulated frame. The adiabaticity of the S^3AP is quantified with an adiabaticity factor $Q_{\mathrm{B}}^{(1)}$, which is defined as

$$\frac{1}{Q_{\mathrm{B}}^{(1)}} = \max \left| \frac{\dot{\theta}_{\mathrm{B}}^{(0)}(t)}{\omega_{\mathrm{eff,B}}^{(0)}(t)} \right|. \tag{120}$$

As previously the pulse is said to be adiabatic when this adiabaticity factor is much greater than unity, here corresponding to $Q_{\mathrm{B}}^{(1)} \gg 1$, in which case we can neglect the last term in $\hat{H}_{\mathrm{B}}^{(1)}(t)$, which now takes the following approximate expression:

$$\hat{H}_{\mathrm{B}}^{(1)}(t) \approx \omega_{\mathrm{eff,B}}^{(0)}(t)\hat{I}_z^{(+1,-1)} + \frac{\omega_1(t)^2}{2\omega_{\mathrm{r}}} c_\Sigma \left[\hat{I}_z^{(+1,0)} - \hat{I}_z^{(0,-1)}\right]. \tag{121}$$

This Hamiltonian is used to evaluate the inversion and refocussing performance of the pulse.

The propagator $\hat{U}_{\mathrm{B}}(t,0)$ is:

$$\begin{aligned}\hat{U}_{\mathrm{B}}(t,0) =& \hat{R}_z\left(\phi_{\mathrm{p}}(t)\right) \hat{U}_{\mathrm{q}}^{\mathrm{Q}}\left(\xi_{\mathrm{q}}^{(0)}\right)^{-1} \hat{R}_y^{(+1,-1)}\left(\theta_{\mathrm{B}}^{(0)}(t)\right) \hat{R}_z^{(+1,-1)} \left(\int_0^t \omega_{\mathrm{eff,B}}^{(0)}(t')\mathrm{d}t'\right) \hat{U}_{\mathrm{q}}^{\mathrm{Q}}\left(\frac{3c_\Sigma}{4\omega_{\mathrm{r}}}\int_0^t \omega_1(t')^2\mathrm{d}t'\right) \\ & \times \hat{U}_{\mathrm{q}}^{\mathrm{Q}}\left(\xi_{\mathrm{q}}^{(0)}\right) \hat{R}_z\left(\phi_{\mathrm{p}}(0)\right)^{-1},\end{aligned} \tag{122}$$

where we have noted that $\theta_{\mathrm{B}}^{(0)}(0) = 0$. The inversion performance is determined by applying $\hat{U}_{\mathrm{B}}(t,0)$ to $\hat{I}_z$, which results in the following density operator:

$$\hat{\rho}(t) = \cos\left(\theta_{\mathrm{B}}^{(0)}(t)\right)\hat{I}_z + 2\sin\left(\theta_{\mathrm{B}}^{(0)}(t)\right)\left[\cos\left(2\phi_{\mathrm{p}}(t)\right)\hat{I}_x^{(+1,-1)} + \sin\left(2\phi_{\mathrm{p}}(t)\right)\hat{I}_y^{(+1,-1)}\right]. \tag{123}$$

At the end of the pulse the tilt angle takes the value $\theta_{\mathrm{B}}^{(0)}(\tau_{\mathrm{p}}) = \pi$, and complete inversion is obtained. However for refocussing the pulse has a more complicated effect. The second term in the Hamiltonian in equation 121, of spherical rank two, is not self-refocussed during a single pulse, and so the excitation-sculpting principle breaks down. The result of a pair of pulses being applied

to $\hat{I}_-$ is the following density operator

$$\hat{\rho}(2\tau_\mathrm{p}) = -\sqrt{2}\left[\hat{I}_-^{(+1,0)}\exp\left(\mathrm{i}\frac{3c_\Sigma}{2\omega_\mathrm{r}}\int_0^{\tau_\mathrm{p}}\omega_1(t)^2\mathrm{d}t\right) + \hat{I}_-^{(0,-1)}\exp\left(-\mathrm{i}\frac{3c_\Sigma}{2\omega_\mathrm{r}}\int_0^{\tau_\mathrm{p}}\omega_1(t)^2\mathrm{d}t\right)\right]. \qquad (124)$$

We see that there are two terms, in $\hat{I}_-^{(+1,0)}$ and $\hat{I}_-^{(0,-1)}$, each of which has acquired an orientation-dependent phase. This effect is not refocussed by the pair of pulses as it is due to the second-rank term in the Hamiltonian. The S^3AP therefore cannot be used to refocus single-quantum coherences of spins $I = 1$ when the quadrupolar interaction is non-negligible.

It is worth considering the refocussing effect of the pulse on the one remaining coherence operator $\hat{I}_-^{(+1,-1)}$ which represents double-quantum coherence. It is straightforward to show that, in both regimes A and B, applying a pair of pulses to $\hat{I}_-^{(+1,-1)}$ results in complete refocussing along the coherence-transfer pathway $-2 \rightarrow +2 \rightarrow -2$ with no overall phase, i.e. $\hat{\rho}(2\tau_\mathrm{p}) = \hat{I}_-^{(+1,-1)}$. Therefore we can use the S^3AP to refocus double-quantum coherences.

Before leaving this topic we make a comment about the adiabaticity factors. When optimizing an adiabatic pulse for inversion on an isotropic spin system it is necessary to increase the adiabaticity factor so that it passes a well-defined threshold value, that depends on the pulse length, sweep width, and RF field amplitude [5]. Therefore it follows that if this minimum adiabaticity factor is known the required pulse parameters can be calculated rather than optimized. The same principles are true for an S^3AP applied to an anisotropic spin $I = 1$, but with the additional complication that the adiabaticity factors in the two pulse regimes A and B, given by Equations 109 and 120, now depend on the quadrupolar spin parameters, crystallite orientation (via $B_\mathrm{q}^{(0)}$ and c_Σ), and MAS frequency in addition to the parameters defining the pulse. This means that whilst it may be possible to calculate the threshold pulse parameters required for inversion of the spin in a crystallite of a particular orientation, doing the same for a powder sample is a more difficult task since we must now consider a range of values of $B_\mathrm{q}^{(0)}$ and c_Σ for different crystallites. Furthermore we recall that different crystallites may be in different regimes A and B for a given RF field amplitude. In practice this means that for a powder sample it is a simpler task to optimize the S^3AP experimentally, than to calculate the optimum parameters.

VI. THE THEORETICAL DESCRIPTION OF PULSE SCHEMES FOR LOW-POWER DOUBLE-QUANTUM EXCITATION FOR SPIN $I = 1$ IN PRESENCE OF FIRST-ORDER QUADRUPOLAR INTERACTION

We now turn to the second topic of this paper, which is the use of low-power single-sideband-selective irradiation schemes to excite double-quantum coherences. This is of interest as such coherences do not evolve under the first-order quadrupolar interaction, and so exhibit higher resolution in the spectrum. To describe the double-quantum excitation schemes at low power we again extend the jolting-frame formalism, and give particular attention to the double-quantum RF field term in the effective Hamiltonian of equation 97. We then use the theory to design an entirely new low-power pulse scheme that can be used to generate double-quantum coherences with unprecedented efficiency.

A. The jolting-frame description

We begin the development of a double-quantum excitation pulse sequence with the analysis of a conventional low-power pulse of constant amplitude ω_1 and phase ϕ_p that is resonant with the centreband. We also take the duration of the pulse to be one rotor period τ_r, and employ stroboscopic sampling where we observe the density operator only at multiples of τ_r. Under these conditions, and with the only time dependence in the jolting frame being due to the MAS modulation of the quadrupolar interaction, the evolution of the spin system is properly described with AHT. The first three lowest-order average Hamiltonians are described by equations 55–57, using the expression for $\hat{h}_p$ given in equation 87.

The first- and second-order average Hamiltonians $\overline{H}^{(1)}_{\phi_\mathrm{p}}$ and $\overline{H}^{(2)}_{\phi_\mathrm{p}}$ are given by equations 55 and 56, and have the forms:

$$\overline{H}^{(1)}_{\phi_\mathrm{p}} = \omega_1 B^{(0)}_\mathrm{q} \hat{R}_z\left(\phi_\mathrm{p}\right) \hat{U}^\mathrm{Q}_\mathrm{q}\left(\xi^{(0)}_\mathrm{q}\right)^{-1} \hat{I}_x \hat{U}^\mathrm{Q}_\mathrm{q}\left(\xi^{(0)}_\mathrm{q}\right) \hat{R}_z\left(\phi_\mathrm{p}\right)^{-1}, \tag{125}$$

$$\overline{H}^{(2)}_{\phi_\mathrm{p}} = \frac{\omega_1^2}{2\omega_\mathrm{r}} d_\Sigma \left[\hat{I}_z^{(+1,0)} - \hat{I}_z^{(0,-1)} + \hat{R}_z\left(\phi_\mathrm{p}\right) \hat{I}_x^{(+1,-1)} \hat{R}_z\left(\phi_\mathrm{p}\right)^{-1}\right]. \tag{126}$$

The first-order average Hamiltonian has exactly the same form as the first-order effective Floquet Hamiltonian, as both are equal to $\hat{h}_0$, and comprises single-quantum spin operators. The second-order average Hamiltonian comprises longitudinal and double-quantum spin operators, and has

the same form as the second-order effective Floquet Hamiltonian, but with c_Σ substituted with d_Σ, which has the expression

$$d_\Sigma = \sum_{p\neq 0}\left[\frac{\left(B_{\mathrm{q}}^{(+p)}\right)^2 - \left(B_{\mathrm{q}}^{(-p)}\right)^2 - 2B_{\mathrm{q}}^{(0)}B_{\mathrm{q}}^{(+p)}\cos\left(\xi_{\mathrm{q}}^{(+p)} - \xi_{\mathrm{q}}^{(0)}\right) + 2B_{\mathrm{q}}^{(0)}B_{\mathrm{q}}^{(-p)}\cos\left(\xi_{\mathrm{q}}^{(-p)} - \xi_{\mathrm{q}}^{(0)}\right)}{p}\right]. \quad (127)$$

The double-quantum part of $\overline{H}^{(2)}_{\phi_\mathrm{p}}$ is of interest here as it can be used to excite double-quantum coherences.

The expression for $\overline{H}^{(1)}_{\phi_\mathrm{p}}$ is proportional to the operator $\hat{I}_x$ under a unitary transformation. From the transformation rules summarized in the SI, this Hamiltonian can be written as a sum of the coherence operators $\hat{I}_\pm^{(+1,0)}$ and $\hat{I}_\pm^{(0,-1)}$, each of which is subject to a phase shift. In particular each of these coherence operators is shifted by a phase $\mp\phi_\mathrm{p}$ imparted by the pulse, as can be seen directly from the expression for $\hat{h}_0$ given by equation 87. In the second-order average Hamiltonian the longitudinal operators are independent of the pulse phase, whilst the double-quantum operators $\hat{I}_\pm^{(+1,-1)}$ have phase $\mp 2\phi_\mathrm{p}$. This arises because $\overline{H}^{(2)}_{\phi_\mathrm{p}}$ is calculated from commutators of the form $\left[\hat{h}_r, \hat{h}_q\right]$, the products of which have phase factors either of the form $\exp\left[\pm\mathrm{i}(\phi_\mathrm{p} - \phi_\mathrm{p})\right] = 1$ or $\exp\left[\pm\mathrm{i}(\phi_\mathrm{p} + \phi_\mathrm{p})\right] = \exp\left[\pm\mathrm{i}2\phi_\mathrm{p}\right]$.

The expression for the third-order average Hamiltonian $\overline{H}^{(3)}_{\phi_\mathrm{p}}$ is more complicated, but we are able to elucidate the dependence on ϕ_p rather easily using the approach above. From equation 57 we see that the third-order average Hamiltonian depends on double commutators of the form $\left[\hat{h}_s, \left[\hat{h}_r, \hat{h}_q\right]\right]$. The phase factors of this expression are therefore calculated from the product of a phase factor of $\hat{h}_s$ with a phase factor of $\overline{H}^{(2)}_{\phi_\mathrm{p}}$, which gives overall phases of $\pm\phi_\mathrm{p}$ and $\pm 3\phi_\mathrm{p}$. However we note that the latter phase corresponds to a triple-quantum spin operator which cannot be generated for a single spin $I = 1$, for which only orders between -2 and $+2$ can be generated. That is to say the basis operators representing a single spin $I = 1$ comprises orders of only up to double quantum. Therefore the third-order average Hamiltonian contains only single-quantum terms with phases imparted by the pulse of $\pm\phi_\mathrm{p}$.

B. The XiX double-quantum excitation pulse sequence

Having established the forms of the average Hamiltonians and how they vary with the pulse phase, we now require a pulse scheme in which the double-quantum part of $\overline{H}^{(2)}_{\phi_\mathrm{p}}$ is retained, and

any undesirable remaining terms are suppressed. This is because the generation of double-quantum coherence is due to evolution under the double-quantum Hamiltonian, whilst the remaining terms may result in transformations to other, unwanted coherences. To achieve our aim we exploit the different phase properties of the average Hamiltonians. In particular we see that when the phase is inverted from $\phi_\mathrm{p} = 0$ to π, the odd-order average Hamiltonians undergo a sign change, whilst the even-order average Hamiltonians are unchanged. If we denote the rth-order Hamiltonian with phase 0 and π as $\overline{H}^{(r)}_{+x}$ and $\overline{H}^{(r)}_{-x}$ respectively we summarise these symmetry properties as:

$$\overline{H}^{(r)}_{-x} = (-1)^r \overline{H}^{(r)}_{+x}. \tag{128}$$

From here we see that we can eliminate the first-order average Hamiltonian by constructing a supercycle comprising a pair of pulses S_{+x} and S_{-x} of the same length τ_r and phases 0 and π [55]. The evolution of the density operator over this supercycle of total length $2\tau_\mathrm{r}$ is described by an average Hamiltonian $\overline{H}_{x-x}$, which can be calculated from the average Hamiltonians of the two pulses $\overline{H}_{+x}$ and $\overline{H}_{-x}$ using the Baker–Campbell–Hausdorff expansion [49]:

$$\exp\left(-\mathrm{i}\overline{H}_{x-x}2\tau_\mathrm{r}\right) = \exp\left(-\mathrm{i}\overline{H}_{-x}\tau_\mathrm{r}\right)\exp\left(-\mathrm{i}\overline{H}_{+x}\tau_\mathrm{r}\right) \tag{129}$$

$$= \exp\left[-\mathrm{i}\left(\overline{H}_{-x} + \overline{H}_{+x}\right)\tau_\mathrm{r} - \frac{1}{2}\left[\overline{H}_{-x}, \overline{H}_{+x}\right]\tau_\mathrm{r}^2 + \ldots\right]. \tag{130}$$

This gives the following expression:

$$\overline{H}_{x-x} = \frac{1}{2}\left(\overline{H}_{-x} + \overline{H}_{+x}\right) - \frac{\mathrm{i}\pi}{2\omega_\mathrm{r}}\left[\overline{H}_{-x}, \overline{H}_{+x}\right] + \ldots. \tag{131}$$

Now we expand $\overline{H}_{\pm x}$ as sums of the rth-order Hamiltonians, and obtain the following expression for $\overline{H}_{x-x}$ truncated at third order:

$$\overline{H}_{x-x} = \overline{H}^{(2)}_{+x} + \frac{\mathrm{i}\pi}{\omega_\mathrm{r}}\left[\overline{H}^{(1)}_{+x}, \overline{H}^{(2)}_{+x}\right]. \tag{132}$$

From Equation 132 we see that the first-order average Hamiltonian of the supercycle is zero, and the second-order average Hamiltonian is equal to the second-order term of the single pulse S_{+x}, $\overline{H}^{(2)}_{+x}$. This is a consequence of the symmetry properties in Equation 128. The commutator in Equation 132 represents a cross term between $\overline{H}^{(1)}_{+x}$ and $\overline{H}^{(2)}_{+x}$, and is equal to the third-order

contribution to $\overline{H}_{x-x}$. Substituting in the expressions in Equations 125 and 126 we obtain the following explicit expressions for $\overline{H}_{x-x}$ to up third order:

$$\overline{H}^{(1)}_{x-x} = \hat{0}, \tag{133}$$

$$\overline{H}^{(2)}_{x-x} = \frac{\omega_1^2}{2\omega_\mathrm{r}} d_\Sigma \left[\hat{I}_z^{(+1,0)} - \hat{I}_z^{(0,-1)} + \hat{I}_x^{(+1,-1)}\right], \tag{134}$$

$$\overline{H}^{(3)}_{x-x} = \frac{\pi\omega_\mathrm{r}^3}{\omega_1^2} B_\mathrm{q}^{(0)} d_\Sigma \hat{U}_\mathrm{q}^\mathrm{Q}\left(\pi/2 - \xi_\mathrm{q}^{(0)}\right) \hat{I}_x \hat{U}_\mathrm{q}^\mathrm{Q}\left(\pi/2 - \xi_\mathrm{q}^{(0)}\right)^{-1}, \tag{135}$$

where $\hat{0}$ is the null operator. Henceforth we do not discuss the third-order term further. The remaining second-order average Hamiltonian contains only the second-rank longitudinal spin operator $\hat{I}_z^{(+1,0)} - \hat{I}_z^{(0,-1)}$, and the double-quantum spin operator $\hat{I}_x^{(+1,-1)}$. Following the application of N supercycles the resulting density operator is described by a propagator $\hat{U}_{x-x}(2N\tau_\mathrm{r}, 0)$. Remembering that $\hat{I}_z^{(+1,0)} - \hat{I}_z^{(0,-1)}$ commutes with $\hat{I}_x^{(+1,-1)}$ we write this propagator as the product of two operator exponentials:

$$\hat{U}_{x-x}(2N\tau_\mathrm{r}, 0) = \exp\left[-\mathrm{i}\overline{H}^{(2)}_{x-x} 2N\tau_\mathrm{r}\right] \tag{136}$$

$$= \exp\left[-\mathrm{i}\frac{\omega_1^2}{2\omega_\mathrm{r}} d_\Sigma \hat{I}_x^{(+1,-1)} 2N\tau_\mathrm{r}\right] \exp\left[-\mathrm{i}\frac{\omega_1^2}{2\omega_\mathrm{r}} d_\Sigma \left(\hat{I}_z^{(+1,0)} - \hat{I}_z^{(0,-1)}\right) 2N\tau_\mathrm{r}\right]. \tag{137}$$

We now examine the excitation of double-quantum coherence from equilibrium magnetization by applying $\hat{U}_{x-x}(2N\tau_\mathrm{r}, 0)$ to $\hat{I}_z$. The right-hand operator in equation 137 commutes with $\hat{I}_z$, and so can be neglected. The transformation under the left-hand term can be written in a straightforward manner by using $\hat{I}_z = 2\hat{I}_z^{(+1,-1)}$ and the following transformation rule [33, 35]:

$$\exp\left(-\mathrm{i}\phi\hat{I}_x^{(+1,-1)}\right) \hat{I}_z^{(+1,-1)} \exp\left(+\mathrm{i}\phi\hat{I}_x^{(+1,-1)}\right) = \cos(\phi)\hat{I}_z^{(+1,-1)} - \sin(\phi)\hat{I}_y^{(+1,-1)}. \tag{138}$$

Hence the generation of double-quantum coherence for a single crystallite is governed by the following transformation under $\hat{U}_{x-x}(2N\tau_\mathrm{r}, 0)$:

$$\hat{U}_{x-x}(2N\tau_\mathrm{r}, 0)\, \hat{I}_z \hat{U}_{x-x}(2N\tau_\mathrm{r}, 0)^{-1} = \cos(\varepsilon)\hat{I}_z - 2\sin(\varepsilon)\hat{I}_y^{(+1,-1)}. \tag{139}$$

The magnitude of the double-quantum coherence is $|2\sin(\varepsilon)|$ where ε is a flip angle with the

following expression

$$\varepsilon = 2d_{\Sigma}N\pi\left(\frac{\omega_1}{\omega_r}\right)^2. \tag{140}$$

The efficiency of the double-quantum excitation depends both on the crystallite orientation via the sideband intensities and phases in the expression d_{Σ}, as well as the values of the spinning frequency and RF field amplitude.

This double-quantum creation process has a companion transformation in which double-quantum coherences are converted back to z-magnetization with the same XiX pulse train. The transformation is

$$\hat{U}_{x-x}(2N\tau_r, 0)\left[2\hat{I}_y^{(+1,-1)}\right]\hat{U}_{x-x}(2N\tau_r, 0)^{-1} = 2\cos(\varepsilon)\hat{I}_y^{(+1,-1)} + \sin(\varepsilon)\hat{I}_z. \tag{141}$$

We refer to the double-quantum excitation and reconversion sequences as $z2DQ$ and $DQ2z$ respectively.

Whilst the individual pulses in the XiX sequence are single-sideband selective, it is worth noting that the XiX sequence itself is not. Since the sequence is periodic with cycle time τ_c the excitation profile contains sidebands located at frequencies $n\omega_c$ relative to the carrier, where $\omega_c = 2\pi/\tau_c$ and n is an integer, which is analogous behaviour to the DANTE sequence [3, 4]. For all the XiX sequences here τ_c is equal to two rotor periods, and so the sidebands are separated by half the spinning frequency. This is a detail that is not immediately apparent in the average-Hamiltonian treatment, since the average Hamiltonian describes only the cumulative evolution of the density operator over the entire XiX sequence, and the presence of the sidebands in the excitation profile only appear explicitly if we consider the Hamiltonian during time points *within* the sequence. Nevertheless the cumulative effect of these excitation sidebands do appear in the average Hamiltonian in the sum expression of d_{Σ}, and clearly both descriptions ultimately give the same description of the spin dynamics.

It is clear that these sequences can be incorporated into a variety of NMR experimental schemes for spin $I = 1$, of which we discuss two. Firstly we apply a pulse sequence that correlates the double-quantum spectrum with the conventional single-quantum spectrum using the sequence and coherence-transfer pathway in Figure 2 (a). The double-quantum coherences are excited using the $z2DQ$ sequence, and then evolve during t_1. The reconversion sequence $DQ2z$ converts these coherences back to z polarization, from which the single-quantum coherences are then excited

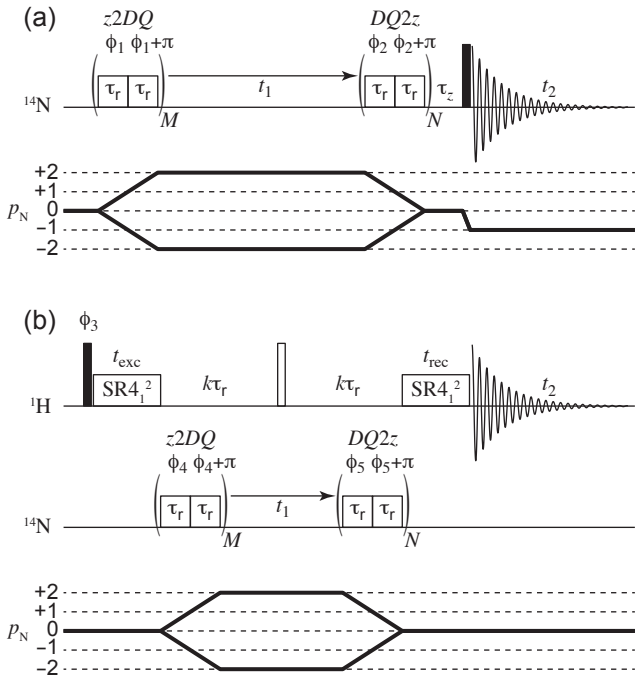

FIG. 2: Examples of pulse sequences and coherence-transfer pathways for correlation spectroscopy for a nuclear spin $I = 1$, employing the XiX double-quantum generation scheme. The two-dimensional double quantum–single quantum correlation pulse sequence is shown in (a). XiX irradiation is used both for double-quantum excitation (z2DQ) and reconversion each to $\hat{I}_z$ (DQ2z). Each RF irradiation period comprises M and N pairs of pulses respectively. The double-quantum evolution occurs during the incremented delay t_1. Following the reconversion irradiation period is a delay τ_z which precedes the final excitation pulse. The element is analogous to a conventional z-filter. Acquisition of the single-quantum spectrum occurs during the time t_2. The pulse phases ϕ_1 and ϕ_2, and receiver phase ϕ_{rx}, are cycled according to an EXORCYCLE scheme [56], i.e. $\phi_1 = (x, y, -x, -y)_4$, $\phi_2 = (x_4, y_4, -x_4, -y_4)$, and $\phi_{\mathrm{rx}} = 2\phi_1 + 2\phi_2$, where the subscript n indicates n repetitions. The D-DQ-HMQC pulse sequence is shown in (b). Here ^{1}H anti-phase coherences are excited by the combination of the first ^{1}H 90° pulse and the symmetry-based heteronuclear diplolar recoupling sequence SR4$^2_1$ [57]. The $\hat{I}_z$ operator on the I-spin is converted into double-quantum coherence with the same XiX sequence as in (a). This double-quantum term then evolves during t_1 before being reconverted back to $\hat{I}_z$. Finally a second SR4$^2_1$ recoupling sequence regenerates the in-phase coherence on ^{1}H that is detected during t_2. The wide unfilled rectangles on the ^{14}N channel represent the low-power single-sideband-selective pulses of length τ_{r}, the narrow filled rectangle is a conventional high-power 90° excitation pulse, and the narrow unfilled rectangle is a conventional high-power 180° refocussing pulse. k is an integer. The pulse and receiver phases are cycled as $\phi_3 = (x_4, y_4, -x_4, -y_4)$, $\phi_4 = (x, y, -x, -y)_4$, $\phi_5 = x_{16}$, and $\phi_{\mathrm{rx}} = 2\phi_4 - \phi_3$.

using a conventional 90° pulse prior to acquisition.

Secondly we present a dipolar-HMQC (D-HMQC) pulse sequence [21–27] that has been modified to acquire the double-quantum spectrum of I indirectly by correlating it with the conventional ^{1}H single-quantum spectrum (hereafter referred to as D-DQ-HMQC). Here the first 90°

pulse excites the ^{1}H coherence $\hat{S}_+$, which evolves during the heteronuclear dipolar recoupling sequence $SR4_1^2$ to generate an anti-phase coherence $\hat{I}_z\hat{S}_+$ [57]. As for the sequence in (a) the XiX double-quantum generation sequence converts the I-spin part of this operator into an I-spin double-quantum coherence $\hat{I}_y^{(+1,-1)}\hat{S}_+$ that evolves during t_1. The second XiX scheme regenerates the anti-phase coherence $\hat{I}_z\hat{S}_+$, which evolves back into the in-phase coherence $\hat{S}_+$ that is detected during acquisition.

Here we note that the scheme of applying a combination of pairs of pulses with phases separated by π has been used for heteronuclear ^{1}H decoupling in the x–inverse x (XiX) scheme [58]. Hence we refer to the present pulse scheme as XiX double-quantum generation/reconversion.

VII. EXPERIMENTAL AND SIMULATION DETAILS

A. Solid-state NMR

Solid-state NMR spectra of $(NH_4)_2C_2O_4$ were acquired on a Bruker Avance III 700 spectrometer operating at a ^{14}N Larmor frequency of 50.6 MHz, with a 3.2 mm HXY probe at 20 kHz MAS. The reference spectra were acquired with a solid-echo pulse sequence (90°–τ_r–90°–τ_r–aqc.), with an EXORCYCLE phase cycle applied to the second pulse [56]. The 90° pulse length was calibrated at 4.88 μs, corresponding to a nominal RF field amplitude of 51.2 kHz. Inverted spectra were acquired with a solid-echo sequence following a WURST-20 S^{3}AP [11, 18] with length 5 ms and sweep width 20 kHz. The spectra were acquired with 512 scans and a recycle delay of 2 s. The double-quantum excitation spectra were acquired with the sequence in Figure 2 (a), to which is appended a solid echo prior to acquisition. The z-filter delay was set to 1 ms. These spectra were acquired with a 64 scans and a recycle delay of 2 s.

Solid-state NMR spectra of glycine were acquired on a Bruker Avance III 500 spectrometer operating at a ^{14}N Larmor frequency of 36.1 MHz, with a 0.7 mm HXY probe at 111.111 kHz MAS. The magic angle was carefully calibrated with a two-dimensional satellite-transition magic-angle spinning (STMAS) spectrum of Na_2SO_4 [59], and it was confirmed that there is negligible drift (< 0.001°) of the angle over time and due to sample ejection/re-insertion. The ^{14}N reference spectra were acquired with a DANTE solid-echo pulse sequence (DANTE–τ_r–DANTE–τ_r–aqc.), with an EXORCYCLE phase cycle applied to the DANTE sequence [56]. The DANTE sequence was a D_1^{41} sequence of duration 41 rotor periods (369 μs), each containing a small-flip-angle pulse

of length 0.0609 μs with a nominal RF field amplitude of 100 kHz. Inverted spectra were acquired with a DANTE solid-echo sequence following a WURST-20 S^3AP [11, 18] with length 1 ms and sweep width 111.111 kHz. The spectra were acquired with 65536 scans and a recycle delay of 1 s. The D-HMQC and D-DQ-HMQC experiments at 111.111 kHz MAS were performed using ^{1}H pulses of lengths 2.5 μs and 5 μs for excitation and refocusing respectively corresponding to an RF field strength of 100 kHz. Heteronuclear ^{1}H–^{14}N dipolar recoupling was achieved with the supercycled symmetry-based recoupling sequence $SR4_1^2$ using experimentally optimized recoupling times of 216 μs and RF field strengths of 79 kHz for both excitation and reconversion [57]. In the D-HMQC experiment the conventional excitation pulses on the ^{14}N channel were optimized experimentally to length of 10 μs using RF field strength of 90 kHz. For the D-DQ-HMQC experiments the pulse sequence in Figure 2 (b) was used with an XiX DQ-generation block that was experimentally optimized to length 72 μs and RF field strength 42 kHz. Each HMQC spectrum was acquired with 128 scans and a recycle delay of 2.0 s.

All spectra were referenced to solid NH_4Cl.

B. SpinDynamica simulations

Spin dynamics simulations were performed using SpinDynamica 2.13.1 in Mathematica 9.0.1.0. The simulations of inversion and refocussing in the presence of an SA interaction, presented in the SI, were performed with an anisotropy of $-\omega_0\Delta\sigma$ of 200 kHz and asymmetry parameter η^{CS} of 0.3 at 60 kHz MAS. Simulations of inversion, refocussing, and double-quantum excitation in the presence of a first-order quadrupolar interaction were performed either with a C_Q of 1.19 MHz (corresponding to $\omega_Q/2\pi = 892.5$ kHz) and asymmetry parameter η_Q of 0.52 at 60 kHz MAS, corresponding to glycine, or with a C_Q of 93.4 kHz ($\omega_Q/2\pi = 70.05$ kHz) and asymmetry parameter η_Q of 0.42 at 20 kHz MAS, corresponding to $(NH_4)_2C_2O_4$. In both cases single-crystal calculations were performed with two representative orientations with Euler angles Ω_{CR} or Ω_{QR} of $(0°, 45°, 0°)$ and $(0°, 60°, 0°)$. Simulations of full powders were performed using the Zaremba–Conroy–Wolfsberg (ZCW) scheme with 538 three-angle sets [60–62].

VIII. EXPERIMENTS AND SIMULATIONS OF LOW-POWER BROADBAND ^{14}N MAS NMR

A. Simulated single-crystal results for S^{3}AP for spin $I = 1$ under first-order quadrupolar interaction

We now turn our attention to the application of an S^{3}AP to the inversion of populations and refocussing of coherences of a spin $I = 1$ subject to a large first-order quadrupolar interaction. These results can be compared with those showing the inversion and refocussing applied to a spin $I = 1$ subject to a large SA, which are given in the SI. Figure 3 shows the RF inversion and refocussing profiles of a WURST-20 S^{3}AP applied to the centreband of the spinning-sideband manifold of two single-crystal orientations. The quadrupolar interaction parameters are set to match those of the ^{14}N spin in glycine, i.e. $C_Q = 1.19$ MHz and $\eta_Q = 0.52$, under 60 kHz MAS. The simulated transformation pathway for inversion is $\hat{I}_z \rightarrow c_z\hat{I}_z$, with the RF inversion profile being given by the plot of c_z against RF field amplitude. In all cases the S^{3}AP is applied to the centreband. The simulated refocussing performance as a function of RF field amplitude, referred to as the RF refocussing profile, is calculated from a pair of such pulses applied to the initial operator $\hat{I}_-$. The simulated transformation is $\hat{I}_- \rightarrow c_+\hat{I}_+ \rightarrow c_-\hat{I}_-$, with the RF refocussing profile being given by the plot of c_- against RF field amplitude. This calculation therefore corresponds to the RF refocussing profile of a double spin echo with two S^{3}APs where phase-cycling has been employed to select the coherence (p)-transfer pathway of $p = -1 \rightarrow +1 \rightarrow -1$. We also show the refocussing profiles for double-quantum coherence from a double spin echo, where the calculated transformation is $\hat{I}_-^{(+1,-1)} \rightarrow c_+^{(+1,-1)}\hat{I}_+^{(+1,-1)} \rightarrow c_-^{(+1,-1)}\hat{I}_-^{(+1,-1)}$, and the calculated profile is given by $c_-^{(+1,-1)}$.

The inversion profiles for the orientations specified by $\Omega_{QR} = (0°, 45°, 0°)$ and $\Omega_{QR} = (0°, 60°, 0°)$ are shown in Figure 3 (a) and (b) respectively. The exact RF profile for the orientation $\Omega_{QR} = (0°, 45°, 0°)$ in Figure 3 (a) shows an increasing extent of inversion with increasing RF field amplitude with 100% efficiency at 40 kHz. It can also be seen that this behaviour closely matches that predicted by the first-order effective Floquet Hamiltonian in the jolting-frame model (equations 91 and 92) at all RF field amplitudes up to 60 kHz, and that inclusion of the second-order effective Floquet Hamiltonian (equations 94 and 95) results in only a very minor correction. This indicates that, in this case, the inversion performance is dictated almost entirely by the first-order RF field in the jolting frame model. From this it would appear that the adiabaticity of the

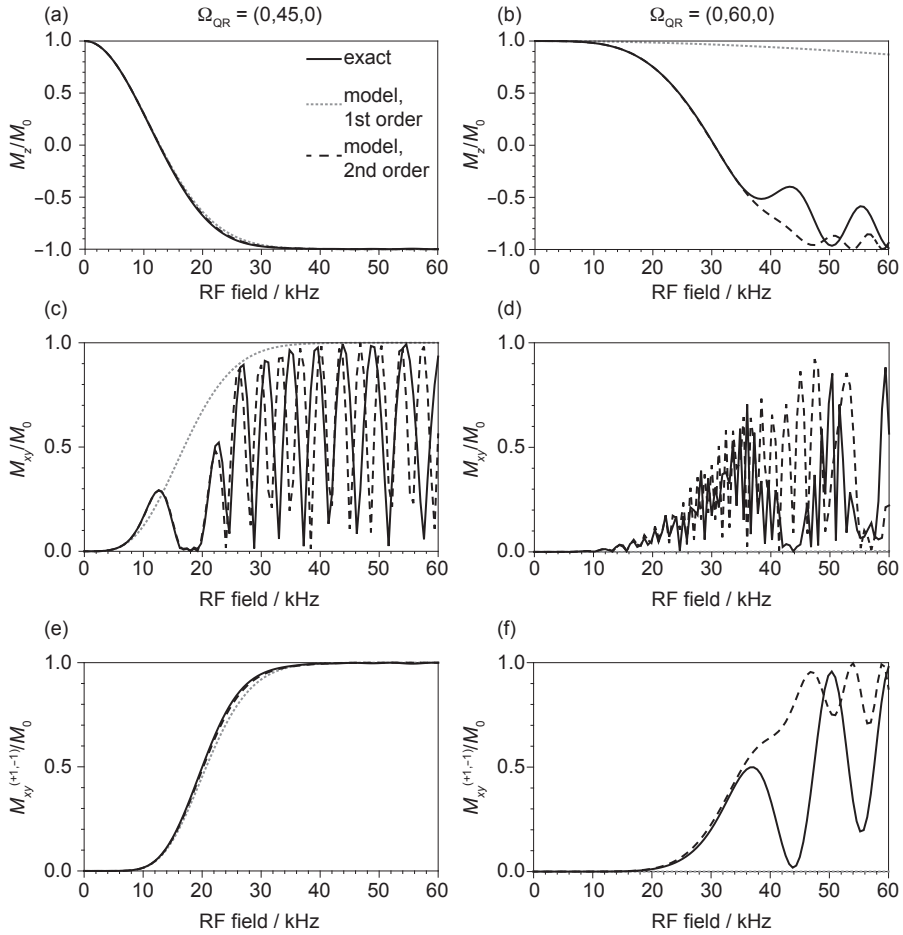

FIG. 3: Simulations of the RF inversion and refocussing profiles of an S^3AP applied to two single-crystal orientations of a spin $I = 1$ subject to an quadrupolar interaction. The crystallite orientation $(0°, 45°, 0°)$ has sideband parameters $B_q^{(0)} = 0.16$ and $c_\Sigma = -0.21$, and the orientation $(0°, 60°, 0°)$ has $B_q^{(0)} = 0.01$ and $c_\Sigma = -0.37$. The two RF inversion profiles, shown in (a) and (b), plot the expectation value of $\hat{I}_z$, M_z/M_0, as a function of RF field amplitude following a single WURST-20 pulse applied to the centreband. In plot (a) complete inversion is obtained with RF field amplitudes above 40 kHz, where the adiabaticity factors in regimes A and B are $Q_A^{(1)} = 4.37$ and $Q_B^{(1)} = 0.39$, indicating that the pulse is operating in regime A. By contrast in plot (b) complete inversion is obtained with RF field amplitudes above 60 kHz, where $Q_A^{(1)} = 0.04$ and $Q_B^{(1)} = 6.44$, indicating that the pulse is operating in regime B. The corresponding single-quantum RF refocussing profiles, shown in (c) and (d) plot the expectation value of $\hat{I}_-$, M_{xy}/M_0, following the application of a pair of the same WURST-20 pulses to the centreband. In this case the coherence-transfer pathway has been filtered to select $p = -1 \rightarrow +1 \rightarrow -1$. The plots in (e) and (f) are double-quantum RF refocussing profiles, which show the expectation value of $\hat{I}_-^{(+1,-1)}$, $M_{xy}^{(+1,-1)}/M_0$, following the application of the pair WURST-20 pulses. Here the selected coherence-transfer pathway is $p = -2 \rightarrow +2 \rightarrow -2$. The results for the crystallite orientation specified by $\Omega_{QR} = (0°, 45°, 0°)$ are shown in (a), (c), and (e), and those for $\Omega_{QR} = (0°, 60°, 0°)$ are shown in (b), (d), and (f). The solid black curves correspond to the exact simulations. The results computed from the jolting-frame approximation are also shown. The dotted grey curves show the results calculated using the first-order effective Hamiltonian (equations 91 and 92), and the dashed black curves show the results calculated from the effective Hamiltonian up to second order (equations 91, 92, 94, and 95). The quadrupole parameters are $C_Q = 1.19$ MHz ($\omega_Q/2\pi = 892.5$ kHz) and $\eta_Q = 0.52$, and the MAS frequency is 60 kHz. The WURST-20 pulse [11] is of 1 ms duration and sweep width 60 kHz, and is applied to the centreband.

S^3AP is described by regime A as defined in equation 100. This observation is supported by a comparison of the adiabaticity factors in the two regimes, which at 40 kHz RF field amplitude are $Q_A^{(1)} = 4.37$ and $Q_B^{(1)} = 0.39$; hence adiabatic behaviour is seen only in regime A. However the actual description of the spin dynamics is more complex, as we will see when discussing the refocussing profiles. What actually happens is that, at higher RF field amplitudes above 10 kHz (i.e. where $\left|\omega_1^{\max}\right| > |\omega_r|/6$) the second-order fields become larger, and their effect is to reinforce the first-order field. The overall spin dynamics actually occur in the cross-over region between regimes A and B, where here the adiabatic behaviour is dominated by the former. This effect is difficult to see here as the inversion performance due to just the first-order field is already very good.

The second profile for the orientation $\Omega_{QR} = (0°, 60°, 0°)$ in Figure 3 (b) shows very different behaviour. Generally whilst the extent of inversion improves on increasing the RF field amplitude, there are two regions (40–45 kHz and 50–55 kHz) were the opposite is seen and the inversion performance is worse. Complete inversion is finally reached at 60 kHz RF field amplitude, where the adiabaticity factors are $Q_A^{(1)} = 0.04$ and $Q_B^{(1)} = 6.44$. This behaviour cannot be explained by the first-order term in the effective Floquet Hamiltonian which, as the simulation shows, results in only a very small field that has a negligible effect on the spin system. On the other hand, including the second-order effective Floquet Hamiltonian results in a better agreement with the exact calculation, indicating that this term dominates the inversion performance at RF field amplitudes of $\left|\omega_1^{\max}\right| > |\omega_r|/6$ (corresponding to a threshold here of 10 kHz), as expected when the adiabatic properties of the pulse are described by regime B in equation 101. The deviation of the jolting frame model from the exact calculation above 40 kHz would be remedied by also including the third-order effective Hamiltonian.

The two RF single-quantum refocussing profiles, shown in Figure 3 (c) and (d), are complicated. This because the quadrupolar coupling Hamiltonian is of spin-rank two, which renders the excitation-sculpting principle invalid, resulting in their being no simple relationship between the inversion and refocussing profiles, unlike the case of the SA, as shown in the SI. However at low RF field amplitudes of $\left|\omega_1^{\max}\right| \leq |\omega_r|/6$, when the spin dynamics are described solely by the first-order effective Floquet Hamiltonian the excitation sculpting principle is still valid as this effective Hamiltonian is of spin-rank one in the adiabatic reference frames. However at higher RF field amplitudes such that $\left|\omega_1^{\max}\right| > |\omega_r|/6$, the increasing size of the spin-rank-two second-order effective Hamiltonian causes the excitation sculpting principle to break down, and results in oscillations in

the refocussing profile that are clearly seen in both Figure 3 (c) and (d). These oscillations indicate that at RF field amplitudes above 10 kHz we depart from regime A, and begin to move towards regime B.

The two refocussing profiles for the double-quantum coherence are shown in Figure 3 (e) and (f). They both exhibit a refocussing efficiency that matches the inversion performance, and 100% efficiency is observed under the same conditions where we obtain complete inversion. The reason for this is that the rank-two second-order Floquet Hamiltonian does not influence the evolution of the double-quantum coherence operators $\hat{I}_{\pm}^{(+1,-1)}$.

The specific simulated examples presented here illuminate some general principles that are relevant when applying S^3APs to spin $I = 1$ nuclei in single-crystals:

- The spin dynamics of an S^3AP can be described by the first-order effective Floquet Hamiltonian in the jolting frame for RF field amplitudes $\left|\omega_1^{\max}\right| \leq \omega_r/6$;
- In the range of RF field amplitudes $\omega_r/6 \leq \left|\omega_1^{\max}\right| \leq \omega_r$ the spin dynamics can be described by an effective Floquet Hamiltonian up to second- or third-order;
- S^3APs can be used for refocussing single-quantum coherences in the absence of a quadrupolar interaction (e.g. for spins $I = 1$ in cubic environments), but not if the quadrupolar interaction is non-negligible;
- S^3APs can always be used for refocussing double-quantum coherences.

B. Experimental and simulated powder-sample results for S^3AP for spin $I = 1$ under first-order quadrupolar interaction

We now present the first experimental applications of the S^3AP to the population inversion of a nuclear spin $I = 1$ subject to a large quadrupolar interaction. Two examples are given, in which we target the ^{14}N nucleus of two different compounds. The first example is the ammonium salt $(NH_4)_2C_2O_4$ under moderate MAS of 20 kHz. The ^{14}N nucleus of the NH_4^+ group experiences a small quadrupolar interaction with $C_Q = 93.4$ kHz and $\eta_Q = 0.42$ [63]. The second example is glycine, in which the ^{14}N of the NH_3^+ group experiences an interaction that is an order of magnitude larger, with $C_Q = 1.19$ MHz and $\eta_Q = 0.52$. To enable efficient excitation and inversion of this ^{14}N spin we employed the 0.7 mm ultra-fast spinning probe at MAS frequencies greater than 100

kHz. In both cases we obtain either complete, or close to complete, inversion using modest RF field amplitudes that are lower than the MAS frequency.

The simulated RF inversion profiles, following irradiation of different sidebands, of $(NH_4)_2C_2O_4$ at 20 kHz MAS are shown in Figure 4 (a). The S^3AP was a WURST-20 pulse with a sweep width that was set to the MAS frequency of 20 kHz, and length 5 ms [11]. Close to 100% inversion is predicted with RF field amplitudes between 6 kHz and 15 kHz by irradiating any of the sidebands with orders between +2 and −2 inclusive. This is a relatively wide window, corresponding to between 30% and 75% of the MAS frequency, and shows that the pulse is very tolerant to a misset in the RF field amplitude, as occurs for example with RF inhomogeneity. The experimental RF inversion profiles are shown for comparison in Figure 4 (b). The experimental RF profiles were computed from the integrals of the spectra over all spinning sidebands, with the values normalized relative to the integral of the spectrum acquired with no inversion. The quality of the agreement is striking, and shows that the predicted favourable tolerance to a misset in the experimental parameters is also realized in practice. The S^3AP irradiation scheme is therefore very robust. It is worth noting that, when applied to paramagnetic systems, the S^3AP generally delivers an inversion performance that is inferior to that predicted by simulation [4, 18]. This is because the longitudinal relaxation times T_1 and coherence lifetimes T_2' are usually comparable to or shorter than the pulse length, which is the order of 1 ms [8, 10]. However that is not the case here with the ^{14}N nucleus in this diamagnetic system, where the relaxation and dephasing losses are clearly negligible even for a pulse of 5 ms length. The S^3AP scheme is therefore particularly suited to the problem of broadband inversion of ^{14}N in diamagnetic systems.

The ^{14}N NMR spectrum acquired following the greatest degree of inversion, here with irradiation of a first-order sideband with an RF field amplitude of 7.1 kHz, is shown in Figure 4 (d), with the reference spectrum shown in Figure 4 (c) for comparison. It is important to note that the inversion does not distort the relative intensities of the spinning sidebands in the manifold, thus indicating that the pulse is inverting the crystallites with different orientations with a high degree of uniformity. We recall here that defining the adiabaticity factors properly for a powder sample is not straightforward as we need to consider different sideband intensity parameters for each crystallite orientation. Nevertheless we can give a nominal adiabaticity factor calculated in the absence of quadrupolar interaction effects, which is 39.7 at the optimum RF field strength of 7.1 kHz for this pulse. The fact that this is higher than needed to achieve inversion of an isotropic spin system indicates the extent to which the quadrupolar interaction under MAS weakens the adiabaticity of

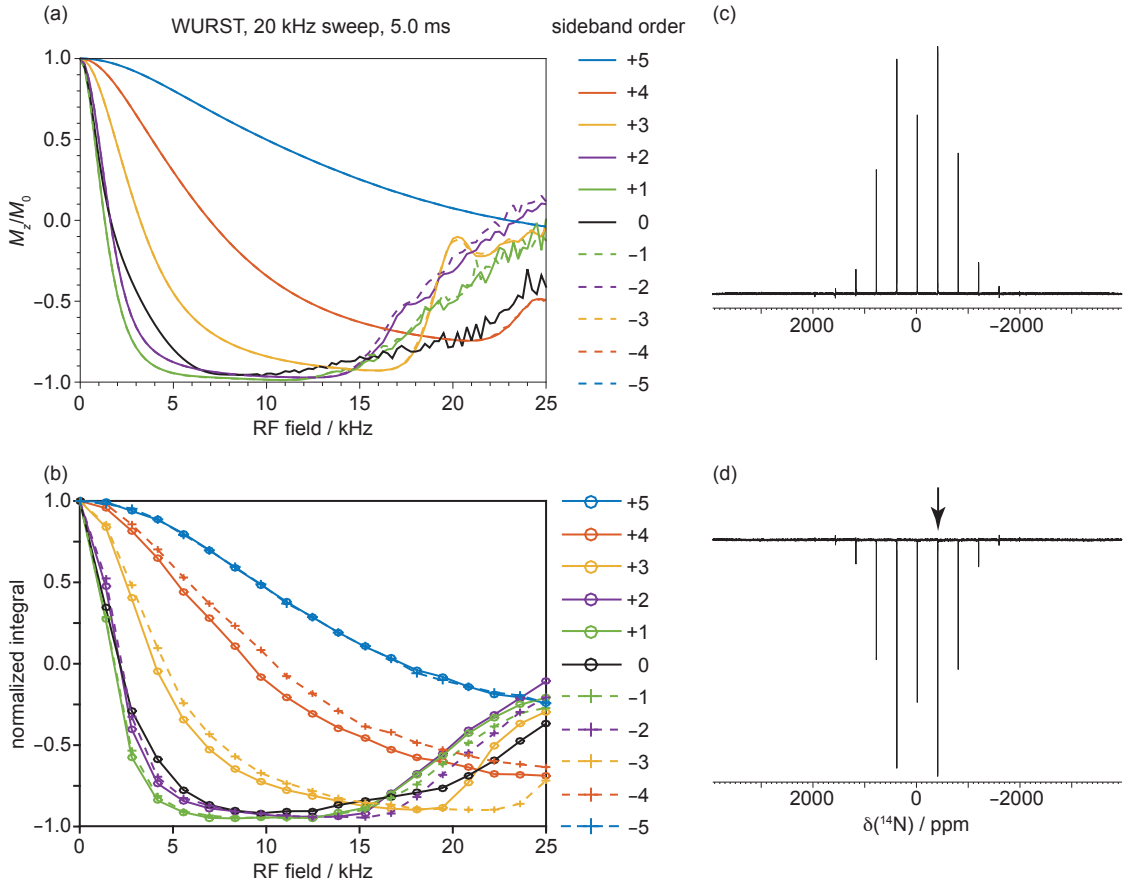

FIG. 4: Evaluation of the inversion performance of a WURST-20 S^3AP acting on a spinning microcrystalline powder sample of $(NH_4)_2C_2O_4$. The simulated RF inversion profiles are shown in (a), and the corresponding experimental profiles are shown in (b). In the latter the data points are computed from the integral over the whole spinning-sideband manifold, and normalizing the values relative to the spectrum acquired following an S^3AP RF field amplitude of zero. In both cases the RF profiles have been determined for irradiation of all the sidebands between orders −5 and +5. The experimental MAS NMR spectra in (c) and (d) were acquired to illustrate the optimum inversion conditions. The reference spectrum is shown in (c). The spectrum following irradiation with a WURST-20 S^3AP is shown in (d), and shows 100% inversion with an optimum RF field amplitude of 7.1 kHz, as determined from the RF inversion profiles shown in (b). The irradiated sideband is indicated with the arrow in (d). The MAS frequency is 20 kHz, and the WURST-20 S^3AP has length 5 ms and sweep width 20 kHz. At the optimum RF field amplitude the adiabaticity factor calculated in the absence of quadrupolar interaction effects is 39.7. The simulated profiles were calculated with a C_Q of 93.4 kHz ($\omega_Q/2\pi$ = 70.05 kHz) and η_Q = 0.42, corresponding to the parameters for $(NH_4)_2C_2O_4$. The powder averaging was performed with 538 ZCW angles [60–62]. See text for further experimental details.

the pulse.

The application of the S^3AP to glycine represents a more exacting test of the method due to the larger quadrupolar interaction. We note that the use of faster sample spinning increases the range

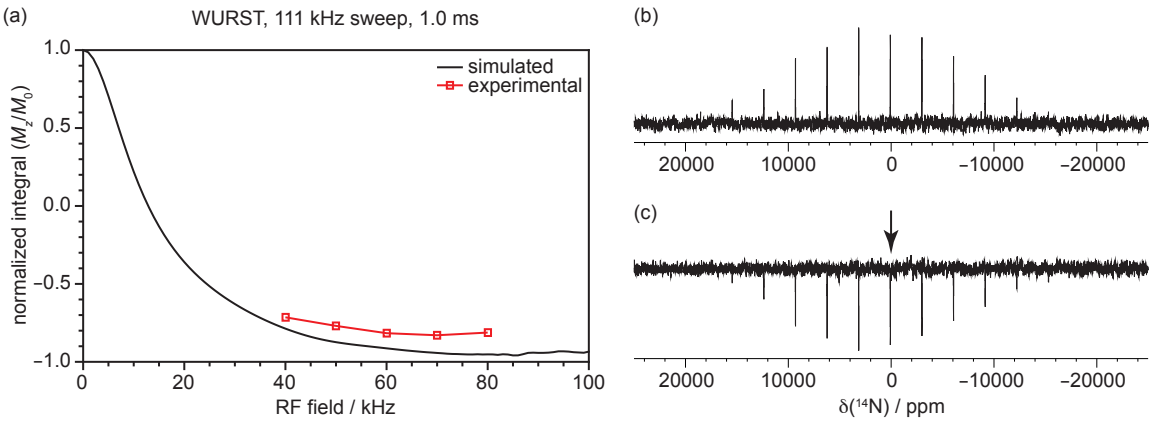

FIG. 5: Evaluation of the inversion performance of a WURST-20 S^3AP acting on a spinning microcrystalline powder sample of glycine. The simulated and experimental RF profiles shown in (a) show the effect of irradiation of the centreband. In the latter the data points are computed from the integral over the whole spinning-sideband manifold, and normalizing the values relative to the spectrum acquired following an S^3AP RF field amplitude of zero. The MAS frequency is 111.111 kHz, and the WURST-20 S^3AP has length 1 ms and sweep width 111.111 kHz. The experimental ^{14}N MAS NMR spectra of glycine are also shown. The reference spectrum at 111.111 kHz MAS is shown in (b). The spectrum following irradiation with a WURST-20 S^3AP is shown in (c), and shows 80% inversion with an optimum RF field amplitude of 70 kHz, as determined by experimental optimization in (a). At this optimum RF field amplitude the adiabaticity factor calculated in the absence of quadrupolar interaction effects is 277. The irradiated sideband was the centreband, as indicated by the arrow in (c). The simulated profiles were calculated with a C_Q of 1.19 MHz ($\omega_Q/2\pi$ = 892.5 kHz) and η_Q = 0.52, corresponding to the parameters for glycine. The powder averaging was performed with 538 ZCW angles [60–62]. See text for further experimental details.

of RF field amplitudes that are still within the low-power approximation. In turn this enables us to employ shorter S^3APs with a larger sweep width, and still attain the adiabatic condition by using a higher RF field amplitude. The shorter pulse length results in less signal loss due to relaxation and coherence dephasing, whilst the wider sweep width results in the pulse inverting over a greater isotropic bandwidth, and therefore a larger isotropic shift dispersion. However the combination of a shorter S^3AP with ultra-fast spinning delivers impressive results as shown by the experimental and simulated inversion profiles in Figure 5 (a). The data were acquired following irradiation of the centreband with a pulse in which the sweep width was set to the MAS frequency of 111.111 kHz, had length 1 ms, and an RF field amplitudes of 40–80 kHz. We obtain a high degree of 80% inversion with an optimum RF field amplitude of 70 kHz. The deviations from the simulation observed here can be ascribed to the faster T_1 relaxation and T_2' dephasing observed for glycine compared to $(NH_4)_2C_2O_4$. The experimental result is impressive since the spectrum, shown in Figure 5 (b), has a broad spinning-sideband manifold with a width of approximately 2 MHz. The

optimum inverted spectrum is shown in Figure 5 (c). As for the previous example we can quote a nominal adiabaticity factor for this pulse in the absence of the anisotropic spin interactions, which for this pulse is 277 at 70 kHz RF field amplitude. Once again we note that the high factor required to achieve inversion of this ^{14}N spin is indicative of how much the adiabaticity is weakened by the quadrupolar interaction.

The results presented here show that the S^{3}AP is capable of ^{14}N population inversion with very impressive efficiencies of up to 100% in the best cases, at low RF field amplitudes of between 30% and 60% of the MAS frequency. Such a high degree of inversion at these low RF powers is completely unprecedented, and cannot even be routinely obtained using conventional high-power pulses. From these results we can make some general comments about the use of S^{3}APs to spin $I = 1$ quadrupolar nuclei in powder samples:

- The S^{3}AP can be used to completely invert a spinning-sideband manifold of a spectral width that is 1–2 orders of magnitude greater than the RF field amplitude;
- The performance of the pulse improves with faster MAS, allowing higher RF field amplitudes and sweep widths to be used. The latter results in a larger inversion bandwidth of isotropic shifts, and also allows complete inversion to be obtained for larger C_Q values;
- The sweep width of the pulse is always set so that it is equal to the MAS frequency;
- The following considerations apply when choosing the length of the pulse. Longer pulses result in the adiabatic condition being reached at lower RF field amplitudes, whereas shorter pulses mitigate relaxation and dephasing losses. The choice represents a compromise between these two factors;
- A full parameter optimisation of the pulse is straightforward, requiring the variation of both the RF field amplitude and the irradiated sideband;
- However if insufficient time is available for a full parameter optimisation, it suffices to irradiate the most intense sideband and vary the RF field amplitude up to a maximum value that is equal to the spinning frequency.

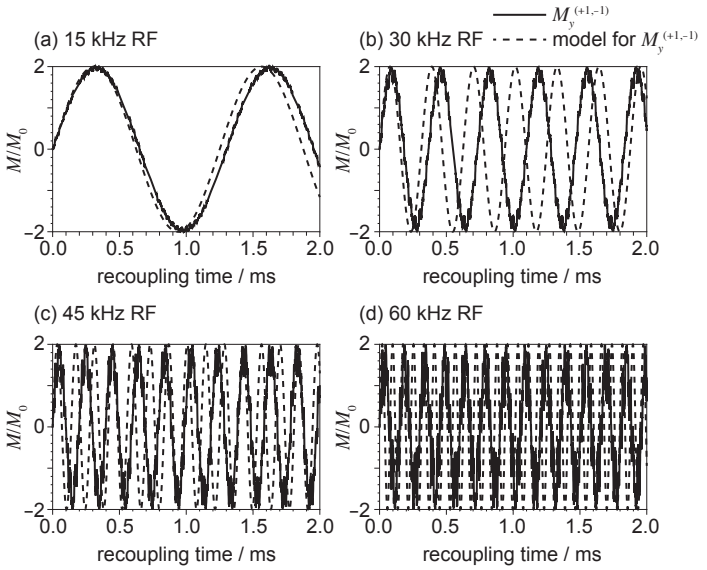

FIG. 6: Simulations of the XiX double-quantum excitation sequence $z2DQ$ on a single-crystal orientation. The quadrupolar spin parameters match those of glycine at 60 kHz MAS, and the single crystal orientation is specified by the Euler angles $\Omega_{\mathrm{QR}} = (0°, 45°, 0°)$. All the plots show the expectation values of $\hat{I}_x^{(+1,-1)}$ and $\hat{I}_y^{(+1,-1)}$ (labelled M/M_0), following the application of the sequence to $\hat{I}_z$, as a function of irradiation time for different RF field amplitudes. The RF field amplitudes are (a) 15, (b) 30, (c) 45, and (d) 60 kHz. Exact calculations of $\hat{I}_y^{(+1,-1)}$ are shown by the solid curves. The dashed curves are calculated from the jolting-frame model to second order, using equations 139 and 140. The quadrupole parameters are $C_Q = 1.19$ MHz ($\omega_{\mathrm{Q}}/2\pi = 892.5$ kHz) and $\eta_{\mathrm{Q}} = 0.52$, and the MAS frequency is 60 kHz.

C. Simulated single-crystal results for double-quantum excitation of a spin $I = 1$ under a first-order quadrupolar interaction

We now turn to the second topic in broadband solid-state NMR of spins $I = 1$, which is the low-power excitation of double-quantum coherences. The excitation scheme that we have developed and the model used to describe it have focussed on the properties of the sequence when applied to a single spinning crystal, and so this is the case we examine first before looking at the excitation applied to a powder sample. Figure 6 shows a series of plots of the simulated amplitude and phase of the double-quantum coherence that is excited for the ^{14}N nucleus of a single crystal of glycine with orientation $\Omega_{\mathrm{QR}} = (0°, 45°, 0°)$ at 60 kHz MAS, and with varying RF field amplitudes. In each case the simulated transformation is $\hat{I}_z \rightarrow c_x^{(+1,-1)}\hat{I}_x^{(+1,-1)} + c_y^{(+1,-1)}\hat{I}_y^{(+1,-1)}$, and the graphs plot the coefficients $c_x^{(+1,-1)}$ and $c_y^{(+1,-1)}$ as a function of irradiation time. Our model predicts that, up to third-order in the average Hamiltonian treatment, an XiX sequence with base phase x excites only $\hat{I}_y^{(+1,-1)}$ with coefficient $c_y^{(+1,-1)} = -2\sin\varepsilon$, where the flip-angle is given by equation 140 as

$\varepsilon = 2d_\Sigma N\pi\,(\omega_1/\omega_r)^2$, with d_Σ given by equation 127, and therefore contains all the information on the spinning sideband intensities and phases, which in turn governs the dependence on orientation of the excitation efficiency. Figure 6 plots the results of the exact simulation, and the jolting frame model for five RF field amplitudes of (a) 15 kHz, (b) 30 kHz, (c) 45 kHz, and (d) 60 kHz.

As expected from the model, only $\hat{I}_y^{(+1,-1)}$ is generated, with an intensity that varies approximately as a sine wave with minimum and maximum values of -2 and $+2$. The agreement between the exact curve for $\hat{I}_y^{(+1,-1)}$ and the second-order jolting-frame model is very good for low RF field amplitudes and moderate irradiation times, such as 1 ms with a 15 kHz RF field. Deviations from the model at higher RF field amplitudes and longer times can be ascribed to the influence of the third- and higher-order average Hamiltonians which we neglect here. Here these terms have the effect of progressively lengthening the peak-to-peak interval in the excitation curves, so that there is no constant period of oscillation, but do not change the maximum excitation intensity. Nevertheless the jolting-frame model to third order accurately predicts all the relevant features of the excitation scheme, in particular the excitation of a double-quantum coherence with uniform phase, and without losing any intensity to the creation of other, unwanted coherences. Therefore the low-power XiX double-quantum excitation scheme $z2DQ$ is an efficient method for when applied to single crystals, with the main advantageous feature being that we are able to excite the maximum possible intensity of double-quantum coherences using an RF field with an amplitude that is an order of magnitude lower than the C_Q parameter.

D. Simulated and experimental powder-sample results for double-quantum excitation of spin $I = 1$ under first-order quadrupolar interaction

We now take the next step in the evaluation of this new low-power sequence, which is to show that double-quantum coherences can be excited with unprecedented efficiency in powder samples. This is potentially challenging since the excitation efficiency for a given RF field amplitude and irradiation time may vary considerably between crystallites with different orientations Ω_{QR}, and so we may expect some cancellation of intensities when we average over the powder. Nevertheless, using a combination of spin dynamics simulations and experimental data on $(NH_4)_2C_2O_4$ at 20 kHz MAS and glycine at 111.111 kHz MAS, we show that high excitation efficiencies for powder samples can be obtained.

We first evaluated the double-quantum excitation sequence for the ^{14}N site of $(NH_4)_2C_2O_4$ at

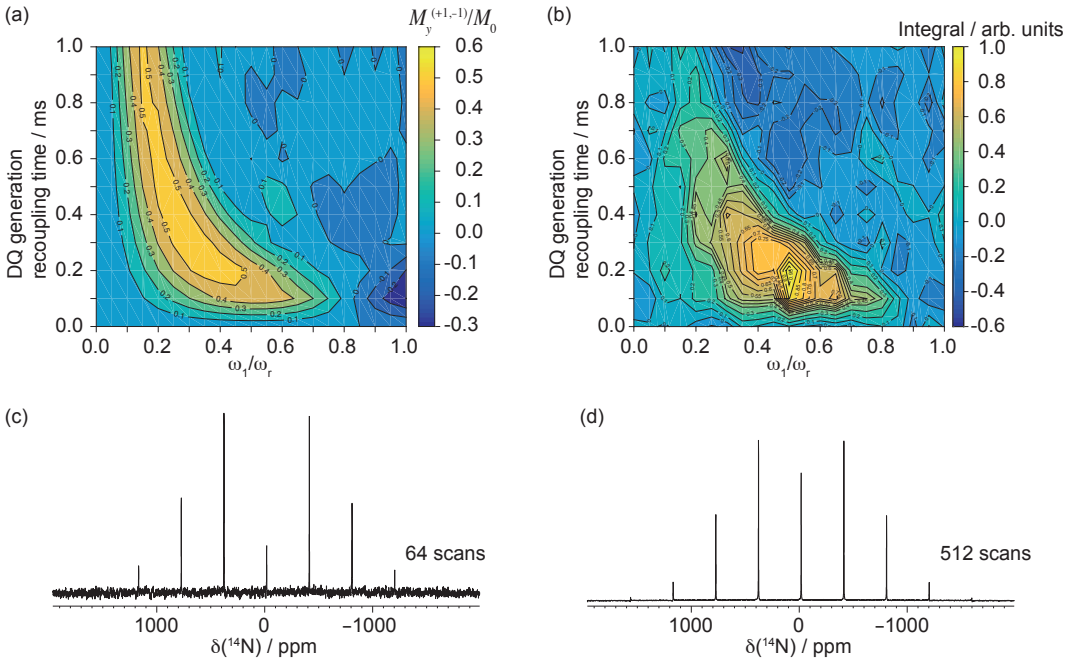

FIG. 7: Experimental and simulated efficiency of the XiX double-quantum generation scheme as a function of RF field amplitude and irradiation time for $(NH_4)_2C_2O_4$ at 20 kHz MAS. The contour plot in (a) shows the simulated double-quantum excitation efficiency of the XiX pulse scheme as a function of total excitation time and RF field amplitude. The equivalent plot is shown in (b), which plots the integral of the total spectral intensity resulting from applying the pulse sequence in Figure 2 (a) with $t_1 = 0$ (and a solid-echo appended immediately prior to acquisition). The optimum experimental values of the excitation time and RF field amplitude were found to be 200 μs and 10 kHz respectively. In acquiring the data shown in (b) the RF field amplitude and duration of the double-quantum reconversion sequence were held constant at the optimum values. The values of the integrals are given relative to the largest value at the optimum experimental parameters. The one-dimensional spectrum resulting from the sequence with the optimum parameters is shown in (c), with the conventional one-dimensional spectrum in (d) for reference. For the simulations the quadrupolar parameters are $C_Q = 93.4$ kHz ($\omega_Q/2\pi = 70.05$ kHz),and $\eta_Q = 0.42$. The powder averaging was performed with 538 ZCW angles [60–62]. See text for further experimental details.

20 kHz MAS using a combination of simulation and experiment. Specifically we investigated the variation of the efficiency of double-quantum excitation on varying the total irradiation time of the XiX sequence and the RF field amplitude. The simulated excitation performance is presented in Figure 7 (a), which presents a contour plot of the intensity of the excited double-quantum coherence, that is the powder average of the coefficient $c_y^{(+1,-1)}$, against these two parameters. We first notice that the highest obtained intensity of the double-quantum coherence is 0.6 which, when compared to the maximum possible of 2.0, corresponds to a maximum theoretical efficiency of 30%. We also see that the region of greatest excitation corresponds to a curve that is reminiscent of a hyperbola, and that there is a large set of parameters which give good double-quantum exci-

tation. As we increase the RF field amplitude the maximum excitation is attained with a shorter irradiation time, as we expect from the form of the flip angle ε which is proportional to $N\omega_1^2$, where N is the number of repeating XiX units. However there is a threshold RF field amplitude, corresponding to approximately $\omega_r/2$, above which the excitation efficiency drops. This can be ascribed to the increasingly important effects of the higher-order terms in the average Hamiltonian and, at sufficiency large RF field amplitudes that are comparable to or greater than the MAS frequency, the breakdown of the low-power approximation. Finally we note that the simulations of the reverse transformation of $\hat{I}_y^{(+1,-1)}$ into $\hat{I}_z$ in the low-power regime produces exactly the same results (not shown). This is expected from the periodic nature of the transformation. An equivalent plot was acquired experimentally using the pulse sequence in Figure 2 (a), with $t_1 = 0$ and a solid-echo sequence appended before acquisition. Here both the irradiation time and RF field amplitude of the XiX double-quantum excitation sequence were varied, while those of the reconversion sequence were left unchanged at 10 kHz and 200 μs, which correspond to the optimum values. The resulting contour plot is shown in Figure 7 (b). We see that whilst the experimental plot qualitatively matches the simulation in Figure 7 (a), there are some quantitative differences, for example in the optimum experimental parameters which are 10 kHz and 200 μs. One possible source for the discrepancy is the instability associated with the sudden change in phase of the pulse in the XiX sequence from 0 to π, which is referred to as a phase transient. This is known to affect adversely the performance of other periodic pulse sequences, such as those used in symmetry-based recoupling [64]. Recently Wittmann et al. have introduced a method to compensate for pulse transients in such sequence [65], which may also be applicable to the present low-power XiX scheme.

The experimental efficiency of the method was determined by computing the signal-to-noise ratio of the sum of the sideband intensities of the spectrum acquired using the optimum excitation and reconversion pulse schemes, shown in Figure 7 (c), and comparing this value with the corresponding signal-to-noise ratio in a reference spectrum, shown in Figure 7 (d), including an adjustment for the different number of scans. The resulting fraction represents the product of the efficiencies of the excitation $z2DQ$ and reconversion $DQ2z$ elements, which are both the same. Therefore the efficiency of both the double-quantum excitation and reconversion elements is given by the square root of this fraction. On performing this calculation we obtain signal-to-noise ratios for the sum of the sidebands that are 134 and 1634 for the double-quantum-filtered and reference spectra respectively. These spectra were acquired with 64 and 512 scans respectively, and so the fraction of intensity retained in the double-quantum-filtered spectrum, adjusted for the dif-

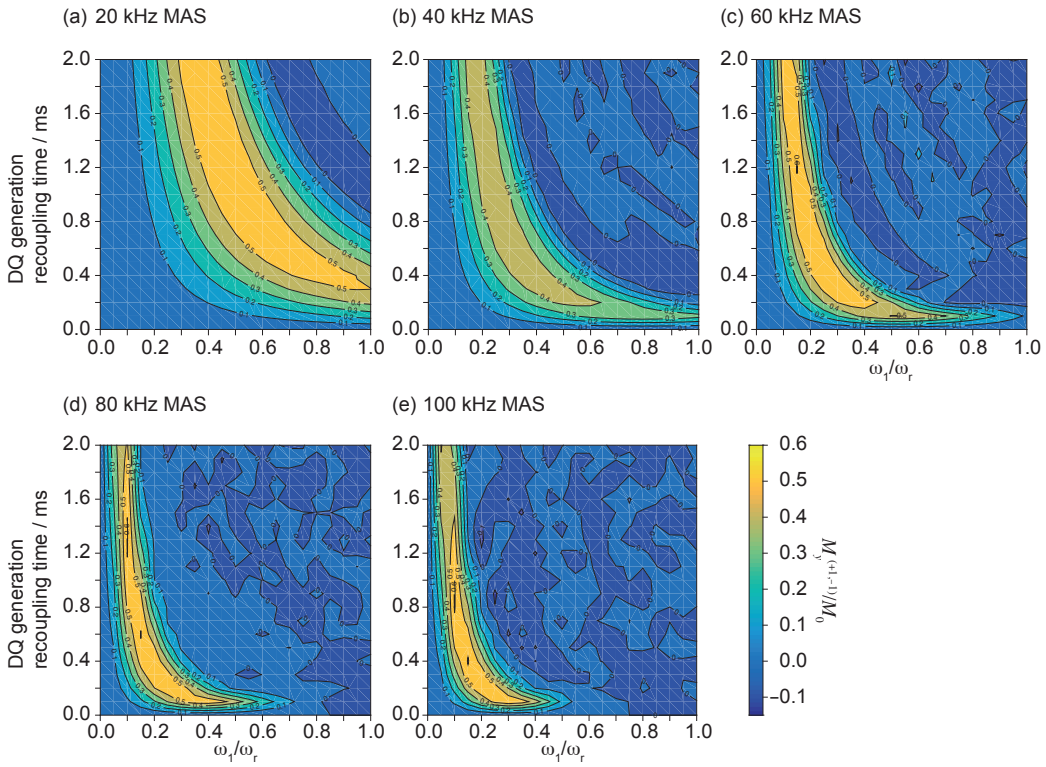

FIG. 8: Simulated contour plots for the generation of ^{14}N double-quantum coherence from a microcrystalline powder of glycine, showing the excitation amplitude as a function of MAS frequency, irradiation time, and RF field amplitude. Each of the five contour plots is computed at a different MAS frequency, and shows the expectation value of the operator $\hat{I}_y^{(+1,-1)}$, $M_y^{(+1,-1)}/M_0$, as a function of irradiation time and RF field amplitude. The MAS frequencies are (a) 20, (b) 40, (c) 60, (d) 80, and (e) 100 kHz. The quadrupolar parameters are C_Q = 1.19 MHz ($\omega_Q/2\pi$ = 892.5 kHz), and η_Q = 0.52. The powder averaging was performed with 538 ZCW angles [60–62].

ferent number of scans, is $(134/1634) \times \sqrt{(512/64)} = 0.23$. Therefore the transfer efficiency for a single double-quantum excitation block is $\sqrt{0.23} = 0.48$, or 48%. This is remarkably high, and completely unprecedented for the low RF field amplitudes, of up to the MAS frequency, utilized here.

We now move onto the second example, which is the more challenging case of glycine at 111.111 kHz MAS. Figure 8 shows the simulated double-quantum excitation efficiency on a powder of glycine with varying irradiation time, RF field amplitude, and MAS frequency. Five simulations were performed, in each of which the irradiation time and RF field amplitude were varied, and the MAS frequency was kept constant. The results are presented as five contour plots in Figure 8 (a)–(e) in which the MAS frequencies are (a) 20 kHz, (b) 40 kHz, (c) 60 kHz, (d) 80 kHz, and (e) 100 kHz. As for the simulation on $(NH_4)_2C_2O_4$ the maximum predicted efficiency is approxi-

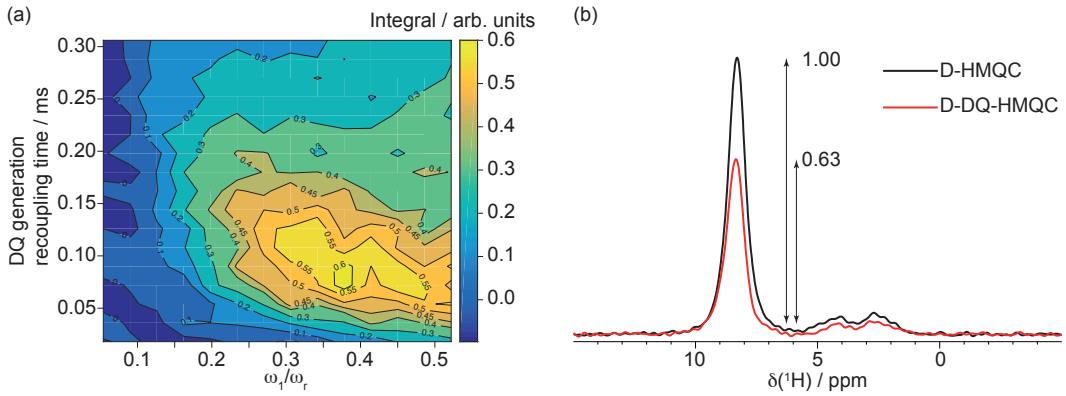

FIG. 9: Experimental evaluation of the XiX double-quantum generation scheme when incorporated into the D-DQ-HMQC pulse sequence in Figure 2 (b) for glycine at 111.111 kHz. The contour plot in (a) shows the experimental double-quantum excitation efficiency of the first XiX block in the D-DQ-HMQC experiment as a function of total excitation time and RF field amplitude. The integrals reported in (a) are those of the $-NH_3^+$ peak in the ^1H spectrum at 8.4 ppm, which is due to the one-bond heteronuclear transfer. The optimum values were found to be 72 μs and 42 kHz respectively. The one-dimensional spectrum resulting from the sequence with the optimum parameters is shown in (b), overlaid with the corresponding spectrum acquired with the conventional D-HMQC spectrum. The broad feature between 1 and 5 ppm is due to a long-range dipolar transfer between ^{14}N and the CH_2 ^1H nuclei. See text for further experimental details.

mately 30% for all MAS frequencies. At faster MAS we see a decrease in the RF field amplitude expressed as fraction of the MAS frequency required to obtain the highest excitation. However the absolute RF field amplitudes required take similar ranges.

The performance of the new double-quantum excitation and reconversion pulse schemes on glycine was evaluated experimentally at 111.111 kHz MAS on the new Bruker 0.7 mm HXY probe. Because of the low sensitivity associated with direct ^{14}N excitation and detection, due to the low gyromagnetic ratio, combined with the small sample volume it proved impractical to perform a full optimization of the excitation time and RF field amplitude using the double quantum–single quantum correlation pulse sequence in Figure 2 (a). We instead used the D-DQ-HMQC sequence in Figure 2 (b) with $t_1 = 0$, which has greater sensitivity due to the excitation and detection of ^1H. The contour plot showing the results of the optimization are shown in Figure 9 (a). The plot shows the variation integral of the peak due to the $-NH_3^+$ group at 8.4 ppm with the parameters of the first XiX block used for double-quantum excitation, with the parameters of the second block unchanged. The optimum excitation efficiency was found with a short excitation time of 72 μs ($N = 4$) and RF field amplitude of 42 kHz. Once again there is good agreement with the results of the simulation shown in Figure 8 (e), but we also note that there is a small quantitative

difference where the experimental optimum RF field amplitude is higher, as was also observed for $(NH_4)_2C_2O_4$.

The efficiency of the D-DQ-HMQC experiment was compared to the conventional D-HMQC. In the latter sequence the two XiX blocks were replaced with two conventional pulses designed to excite ^{14}N single-quantum coherences, whose pulse length and RF field amplitude were optimized experimentally to 10 μs and 90 kHz. An overlay of the first increments of the two optimized spectra, acquired with the same number of scans, is shown in Figure 9 (b). Here we see that the intensity of the peak in D-DQ-HMQC spectrum is 63% of the intensity in the conventional D-HMQC spectrum, which indicates a relative efficiency of each double-quantum excitation block of 79%. This figure is considerably higher than the 30% predicted by the simulation and merits some comment. Firstly the simulation effectively compares the efficiency of the double-quantum excitation relative to a spectrum which represents 100% excitation for all crystallite orientations. This is fundamentally different to the experiment, in which we compare the efficiency of the double-quantum excitation with the efficiency of a conventional ^{14}N excitation pulse which itself does not deliver 100% excitation for all crystallites. Therefore the figure of 79% represents the increased efficiency of the low-power double-quantum excitation scheme compared to a higher power, but not broadband, pulse. This observation is in line with prior studies of broadband NMR with single-sideband-selective pulses [4, 13, 18]. Secondly the simulation also assumes that the crystallite orientations are weighted to reflect a random distribution and that the nuclear spins are at equilibrium prior to excitation. Again this is not the case in the experiment where the contribution from each crystallite to the anti-phase coherence on ^{1}H immediately before double-quantum excitation is also weighted by the orientational dependence of the heteronuclear dipolar recoupling sequence. The crystallites that are more efficiently recoupled are expected to contribute to the intensity of the double-quantum spectrum differently when compared to the statistical average. Nevertheless the observation here is that the excitation efficiencies of the double-quantum excitation scheme when incorporated into the D-HMQC sequence compare very favourably with the conventional experiment at very fast MAS frequencies of more than 100 kHz.

Comparable double-quantum excitation efficiencies using other methods require the application of the highest RF field amplitudes that are available [28, 29]. As a result we expect this new low-power excitation scheme to be widely used.

To finish this section we provide some practical details on the optimisation of this sequence experimentally.

- The full optimisation of the pulse sequence is straightforward, and requires the variation of both the irradiation time and the RF field amplitude.

- The optimal values of both parameters are interdependent, and so both must be varied in a two-dimensional array.

- The irradiation time typically takes an optimum value of the order 100 μs to 1 ms, and the accompanying RF field amplitude optimises within the range of 0 kHz up to the spinning frequency.

- However it is usually sufficient to keep either the RF field amplitude or irradiation time fixed, and to vary the other.

IX. CONCLUSIONS

We have extended the theoretical jolting-frame framework describing low-power solid-state MAS NMR pulse sequences to quadrupolar nuclei of spin $I = 1$, in order to design entirely new methods for obtaining complete population inversion and efficient double-quantum excitation. In the first part of this paper we provided, for the first time, a description of the application of single-sideband-selective adiabatic inversion to spin $I = 1$ quadrupolar nuclei, experiencing a large quadrupolar interaction. Whilst the general concepts closely mirror those presented previously for low-power inversion of spins $I = 1/2$ under a large SA [18], it was also revealed that the increased complexity of the spin $I = 1$ enables us to design entirely new pulse schemes to manipulate other transitions. This finding was exploited in the second part of the paper to design a new double-quantum-excitation pulse scheme that can be incorporated into other experiments.

The inversion and double-quantum pulse schemes were evaluated using a combination of spin-dynamics simulations, and experiments applied to the ^{14}N NMR of both $(NH_4)_2C_2O_4$ and glycine. It was found that, for both the pulse schemes, we are able to manipulate spin systems with anisotropic interactions that are at least one order of magnitude larger than the RF field amplitude. This resulted in very high efficiencies of up to 100% for inversion and 30–79% for double-quantum excitation which for ^{14}N are completely unprecedented at the low RF field amplitudes used here. We have also given a checklist of practical points to aid the spectroscopist in the implementation and optimization of both schemes. It was further shown that the double-quantum

excitation schemes are very versatile and can be incorporated into NMR experiments used to acquire homonuclear double quantum–single quantum correlations, and ^{1}H–^{14}N D-HMQC spectra We expect the pulse schemes presented here to be widely used for ^{14}N and other spin $I = 1$ nuclei, such as ^{2}H. Furthermore following this demonstration of the power of this theoretical method for designing new pulse schemes, we anticipate further advances in the development of NMR methods for numerous applications not only to spins $I = 1$, but also to different and more complex spin systems.

X. SUPPLEMENTARY MATERIAL

See supplementary material for a summary of the different spin operator bases for a spin $I = 1$, a summary of the chemical shielding and paramagnetic shielding interactions of a nuclear spin $I = 1$, a summary of the theory of a S^3AP applied to a spin $I = 1$ subject only to a shielding anisotropy interaction, and simulations of the corresponding RF inversion and refocussing profiles for a single crystal.

XI. ACKNOWLEDGEMENTS

We acknowledge Dr. Dominique Massiot and Dr. Michaël Deschamps (Université d'Orléans), and Prof. Philip J. Grandinetti (Ohio State University) for many useful discussions about various aspects of broadband NMR sequences, adiabaticity, and the jolting frame. AJP also thanks Prof. Malcolm H. Levitt (University of Southampton) for his invaluable support with SpinDynamica, and an interesting discussion regarding some subtle properties of the dynamics of spin-one nuclear spins. AJP and CPG were supported by the Assistant Secretary for Energy Efficiency and Renewable Energy, Office of Vehicle Technologies of the US Department of Energy under Contract DE-AC02-05CH11231, under the Batteries for Advanced Transportation Technologies (BATT) Program Subcontract 7057154. GP acknowledges support from the European Research Council under the European Union's Horizon 2020 Research and Innovation Programme (ERC consolidator Grant 648974 "P-MEM-NMR").

[1] L. A. O'Dell, A. J. Rossini, and R. W. Schurko, Chem. Phys. Lett. **468**, 330 (2009).

[2] L. A. O'Dell and R. W. Schurko, J. Am. Chem. Soc. **131**, 6658 (2009).

[3] V. Vitzthum, M. A. Caporini, S. Ulzega, and G. Bodenhausen, J. Magn. Reson. **212**, 234 (2011).

[4] A. J. Pell and G. Pintacuda, Prog. Nucl. Magn. Reson. Spectrosc. **84-85**, 33 (2015).

[5] M. Garwood and L. DelaBarre, J. Magn. Reson. **153**, 155 (2001).

[6] T. L. Hwang, P. C. M. van Zijl, and M. Garwood, J. Magn. Reson. **133**, 200 (1998).

[7] G. Kervern, G. Pintacuda, and L. Emsley, Chem. Phys. Lett. **435**, 157 (2007).

[8] G. Kervern, S. Steuernagel, F. Engelke, G. Pintacuda, and L. Emsley, J. Am. Chem. Soc. **129**, 14118 (2007).

[9] G. Kervern, A. D'Aleo, O. Maury, L. Emsley, and G. Pintacuda, Angew. Chem. Int. Ed. Engl. **48**, 3082 (2009).

[10] R. J. Clément, A. J. Pell, D. S. Middlemiss, F. C. Strobridge, J. K. Miller, M. S. Whittingham, L. Emsley, C. P. Grey, and G. Pintacuda, J. Am. Chem. Soc. **134**, 17178 (2012).

[11] E. Kupce and R. Freeman, J. Magn. Reson. Ser. A **115**, 273 (1995).

[12] J. Baum, R. Tycko, and A. Pines, Phys. Rev. A **32**, 3435 (1985).

[13] P. Caravatti, G. Bodenhausen, and R. R. Ernst, J. Magn. Reson. **55**, 88 (1983).

[14] R. Siegel, T. T. Nakashima, and R. E. Wasylishen, J. Magn. Reson. **184**, 85 (2007).

[15] K. K. Dey, S. Prasad, J. T. Ash, M. Deschamps, and P. J. Grandinetti, J. Magn. Reson. **185**, 326 (2007).

[16] T. T. Nakashima, R. E. Wasylishen, R. Siegel, and K. J. Ooms, Chem. Phys. Lett. **450**, 417 (2008).

[17] T. T. Nakashima, R. Teymoori, and R. E. Wasylishen, Magn. Reson. Chem. **47**, 465 (2009).

[18] A. J. Pell, G. Kervern, L. Emsley, M. Deschamps, D. Massiot, P. J. Grandinetti, and G. Pintacuda, J. Chem. Phys. **134**, 024117 (2011).

[19] C. P. Grey and W. S. Veeman, Chem. Phys. Lett. **192**, 379 (1992).

[20] C. P. Grey, W. S. Veeman, and A. J. Vega, J. Chem. Phys. **98**, 7711 (1993).

[21] Z. Gan, J. Am. Chem. Soc. **128**, 6040 (2006).

[22] S. Cavadini, A. Lupulescu, S. Antonijevic, and G. Bodenhausen, J. Am. Chem. Soc. **128**, 7706 (2006).

[23] Z. Gan, J. Magn. Reson. **183**, 235 (2006).

[24] Z. Gan, J. Magn. Reson. **184**, 235 (2007).

[25] S. Cavadini, S. Antonijevic, A. Lupulescu, and G. Bodenhausen, ChemPhysChem **8**, 1363 (2007).

[26] Z. Gan, J.-P. Amoureux, and J. Trébosc, Chem. Phys. Lett. **435**, 163 (2007).

[27] S. Cavadini, A. Abraham, and G. Bodenhausen, Chem. Phys. Lett. **445**, 1 (2007).

[28] M. Cutajar, S. E. Ashbrook, and S. Wimperis, Chem. Phys. Lett. **423**, 276 (2006).

[29] S. Cavadini, A. Abraham, S. Ulzega, and G. Bodenhausen, J. Am. Chem. Soc. **130**, 10850 (2008).

[30] L. A. O'Dell and C. I. Ratcliffe, Chem. Phys. Lett. **514**, 168 (2011).

[31] L. A. O'Dell and A. Brinkmann, J. Chem. Phys. **138**, 064201 (2013).

[32] R. R. Ernst, G. Bodenhausen, and A. Wokaun, *Principles of nuclear magnetic resonance in one and two dimensions* (Oxford University Press, Oxford, 1987).

[33] O. W. Sørensen, G. W. Eich, M. H. Levitt, G. Bodenhausen, and R. R. Ernst, Prog. Nucl. Magn. Reson. Spectrosc. **16**, 163 (1983).

[34] H. A. Buckmaster, R. Chatterjee, and Y. H. Shing, Phys. Stat. Sol. A **13**, 9 (1972).

[35] S. Vega, J. Chem. Phys. **68**, 5518 (1978).

[36] M. Mehring, *Principles of High-Resolution NMR in Solids* (Springer Verlag, Berlin, 1983).

[37] S. E. Ashbrook and M. J. Duer, Concept. Magn. Reson. A **28A**, 183 (2006).

[38] M. M. Maricq and J. S. Waugh, J. Chem. Phys. **70**, 3300 (1979).

[39] M. H. Levitt, J. Magn. Reson. **82**, 427 (1989).

[40] P. J. Grandinetti, J. T. Ash, and N. M. Trease, Prog. Nucl. Magn. Reson. Spectrosc. **59**, 121 (2011).

[41] K. F. Riley, M. P. Hobson, and S. J. Bence, *Mathematical Methods for Physics and Engineering* (Cambridge University Press, Cambridge, 1997).

[42] A. J. Pell, G. Pintacuda, and L. Emsley, J. Chem. Phys. **135**, 144201 (2011).

[43] A. J. Pell, R. J. Clément, C. P. Grey, L. Emsley, and G. Pintacuda, J. Chem. Phys. **138**, 114201 (2013).

[44] C. Filip, S. Hafner, I. Schnell, D. E. Demco, and H. W. Spiess, J. Chem. Phys. **110**, 423 (1999).

[45] J. H. van Vleck, Phys. Rev. **74**, 1168 (1948).

[46] H. Primas, Rev. Mod. Phys. **35**, 710 (1963).

[47] M. Goldman, P. J. Grandinetti, A. Llor, Z. Olejniczak, J. R. Sachleben, and J. Zwanziger, J. Chem. Phys. **97**, 8947 (1992).

[48] M. Leskes, P. K. Madhu, and S. Vega, Prog. NMR. Spectrosc. **57**, 345 (2010).

[49] U. Haeberlen and J. S. Waugh, Phys. Rev. **175**, 453 (1968).

[50] E. Kupce and R. Freeman, J. Magn. Reson. Ser. A **118**, 299 (1996).

[51] T. L. Hwang and A. J. Shaka, J. Magn. Reson. Ser. A **112**, 275 (1995).

[52] K. Stott, J. Stonehouse, J. Keeler, T. L. Hwang, and A. J. Shaka, J. Am. Chem. Soc. **117**, 4199 (1995).

[53] D. M. Brink and G. R. Satchler, *Angular Momentum* (Clarendon Press, Oxford, 1993).

[54] M. Deschamps, G. Kervern, D. Massiot, G. Pintacuda, L. Emsley, and P. J. Grandinetti, J. Chem. Phys. **129**, 204100 (2008).

[55] P. E. Kristiansen, M. Carravetta, W. C. Lai, and M. H. Levitt, J. Chem. Phys. **124**, 234510 (2006).

[56] G. Bodenhausen, R. Freeman, and D. L. Turner, J. Magn. Reson. **27**, 511 (1977).

[57] A. Brinkmann and A. P. M. Kentgens, J. Am. Chem. Soc. **128**, 14758 (2006).

[58] A. Detken, E. H. Hardy, M. Ernst, and B. H. Meier, Chem. Phys. Lett. **356**, 298 (2002).

[59] Z. Gan, J. Am. Chem. Soc. **122**, 3242 (2000).

[60] S. K. Zaremba, Ann. Mat. Pura. Appl. **4:73**, 293 (1966).

[61] H. Conroy, J. Chem. Phys. **47**, 5307 (1967).

[62] V. B. Cheng, H. H. Suzukawa, and M. Wolfsberg, J. Chem. Phys. **59**, 3992 (1973).

[63] H. J. Jakobsen, A. R. Hove, R. G. Hazell, H. Bildsøe, and J. Skibsted, Magn. Reson. Chem. **44**, 348 (2006).

[64] M. Edén and M. H. Levitt, J. Chem. Phys. **111**, 1511 (1999).

[65] J. J. Wittmann, K. Takeda, B. H. Meier, and M. Ernst, Angew. Chem. Int. Ed. **54**, 12592 (2015).